Bufe, A., Burbank, D. W., Liu, L., Bookhagen, B., Qin, J., Chen, J., Li, T., Thompson Jobe, J. A., Yang, H. (2017): Variations of Lateral Bedrock Erosion Rates Control Planation of Uplifting Folds in the Foreland of the Tian Shan, NW China. - *Journal of Geophysical Research*, *122*, 12, pp. 2431—2467.

DOI: http://doi.org/10.1002/2016JF004099

AGU PUBLICATIONS

JGR

Journal of Geophysical Research: Earth Surface

RESEARCH ARTICLE
10.1002/2016JF004099

Key Points:
- Rivers in the Tian Shan foreland have repeatedly beveled kilometer-wide surfaces on folds uplifting at 1.0–2.7 mm/yr during the Late Quaternary
- Lateral river erosion rates must change by 1 order of magnitude to explain alternating episodes of planation and incision of folds
- Planation episodes are asynchronous on different folds and likely occur in response to small changes in sediment or water fluxes

Supporting Information:
- Supporting Information S1
- Data Set S1
- Data Set S2

Correspondence to:
A. Bufe,
abufe@gfz-potsdam.de

Citation:
Bufe, A., Burbank, D. W., Liu, L., Bookhagen, B., Qin, J., Chen, J., … Yang, H. (2017). Variations of lateral bedrock erosion rates control planation of uplifting folds in the foreland of the Tian Shan, NW China. *Journal of Geophysical Research: Earth Surface*, *122*, 2431–2467. https://doi.org/10.1002/2016JF004099

Received 20 OCT 2016
Accepted 19 OCT 2017
Accepted article online 9 NOV 2017
Published online 26 DEC 2017

Variations of Lateral Bedrock Erosion Rates Control Planation of Uplifting Folds in the Foreland of the Tian Shan, NW China

Aaron Bufe[1,2,3], Douglas W. Burbank[1,2], Langtao Liu[4,5], Bodo Bookhagen[2,6], Jintang Qin[4], Jie Chen[4], Tao Li[4,7], Jessica A. Thompson Jobe[8], and Huili Yang[4]

[1]Department of Earth Sciences, University of California, Santa Barbara, CA, USA, [2]Earth Research Institute, University of California, Santa Barbara, CA, USA, [3]Now at GFZ German Research Center for Geosciences, Potsdam, Germany, [4]State Key Laboratory of Earthquake Dynamics, Institute of Geology, China Earthquake Administration, Beijing, China, [5]Department of Earth Science and Engineering, Hebei University of Engineering, Handan, China, [6]Institute of Earth and Environmental Science, University of Potsdam, Potsdam, Germany, [7]Department of Earth Sciences, Sun Yat-Sen University, Guangzhou, China, [8]Institute of Tectonic Studies, Department of Geological Sciences, University of Texas at El Paso, El Paso, TX, USA

Abstract Fluvial planation surfaces, such as straths, commonly serve as recorders of climatic and tectonic changes and are formed by the lateral erosion of rivers, a process that remains poorly understood. Here we present a study of kilometer-wide, fluvially eroded, low-relief surfaces on rapidly uplifting folds in the foreland of the southwestern Tian Shan. A combination of field work, digital elevation model analysis, and dating of fluvial deposits reveals that despite an arid climate and rapid average rock-uplift rates of 1–3 mm/yr, rivers cut extensive (>1–2 km wide) surfaces with typical height variations of <6 m over periods of >2–6 kyr. The extent of this "beveling" varies in space and time, such that different beveling episodes affect individual structures. Between times of planation, beveled surfaces are abandoned, incised, and deformed across the folds. In a challenge to models that link strath cutting and abandonment primarily to changes in river incision rates, we demonstrate that lateral erosion rates of antecedent streams crossing the folds have to vary by more than 1 order of magnitude to explain the creation of beveled platforms in the past and their incision at the present day. These variations do not appear to covary with climate variability and might be caused by relatively small (much less than an order of magnitude) changes in sediment or water fluxes. It remains uncertain in which settings variations in lateral bedrock erosion rates predominate over changes in vertical erosion rates. Therefore, when studying fluvial planation and strath terraces, variability of both lateral and vertical erosion rates should be considered.

1. Introduction

Rivers cutting into bedrock commonly record a complex history of vertical incision, aggradation of bed cover, and lateral bedrock erosion that can be interpreted as a result of environmental, tectonic, and autogenic changes. Understanding the formation of landscapes and predicting their evolution under changing climatic and tectonic forcing requires knowledge of these river dynamics. Rivers tend to adjust their channel geometry and their vertical and lateral motion in response to the supply of sediment and water and, in the case of bedrock rivers, to the bedrock-uplift rate (Brocard & van der Beek, 2006; Dietrich et al., 2003; Hack, 1957; Hancock & Anderson, 2002; Kirby & Whipple, 2012; Lague, 2014; Lague et al., 2003; Mackin, 1948; Pazzaglia, 2013; Shepherd, 1972; Sklar & Dietrich, 2001, 2004, 2006; Stark, 2006; Turowski et al., 2008, 2006, 2009; Whipple & Tucker, 2002; Wickert et al., 2013; Wobus et al., 2006; Yanites & Tucker, 2010). This response of the river to external influences allows interpretation of fluvial landscapes as a function of tectonic and climatic drivers (DiBiase & Whipple, 2011; Lague et al., 2003; Langston et al., 2015; Turowski et al., 2006). Ranging from narrow bedrock benches to wide strath terraces and regional planation surfaces, river terraces cut into bedrock are commonly used markers for assessing climatic and tectonic changes in landscapes (Amos et al., 2007; Bookhagen et al., 2006; Burbank et al., 1996; Calvet et al., 2015; Fuller et al., 2009; Hancock & Anderson, 2002; Langston et al., 2015; Lavé & Avouac, 2001; Pazzaglia & Gardner, 1993; Pazzaglia et al., 1998; Pratt-Sitaula et al., 2004). Whereas narrow bedrock benches can form in response to changes solely in channel width, they are rarely preserved as terraces (Pazzaglia, 2013). Here we focus on planation surfaces that are formed in response to the lateral migration of channels. We define a "planation surface" or "strath surface" as a near-planar, river-cut bedrock surface, and a strath terrace as an uplifted

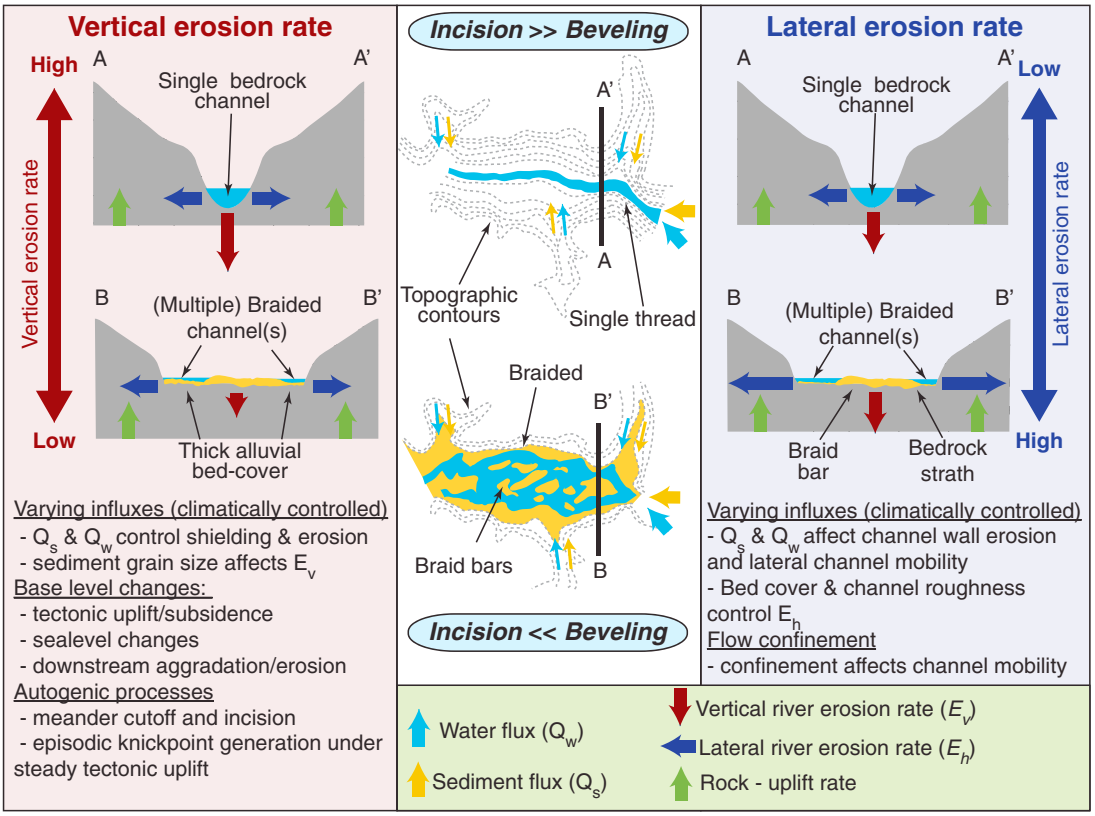

Figure 1. Conceptual sketch of different planation-surface formation models. Changes in the degree of planation can be caused by changing vertical erosion rates and/or changing lateral erosion rates. Different factors controlling lateral and vertical erosion rates are summarized below the sketches. Because the width of planation surfaces is controlled by the ratio of lateral and vertical erosion rates, changes in either one of these rates can lead to similar landforms.

and incised strath surface that includes, where present, a fluvial gravel cover. In order for planar, river-cut surfaces to develop, the lateral erosion by rivers has to balance or outpace vertical river incision (Gilbert, 1877; Hancock & Anderson, 2002; Merritts et al., 1994; Pazzaglia, 2013) (Figure 1). Hence, a decrease in incision rate or an increase in lateral erosion rate can lead to the same landform (Figure 1). Whereas changes in vertical incision rates have repeatedly been measured in the field or modeled with existing bedrock-incision models, the rates, mechanics, and dynamics of lateral bedrock erosion remain poorly understood. Therefore, we lack constraints on the potentially complex interactions between lateral and vertical erosion and their controls on bedrock valley width and strath-terrace formation.

Here, we document extensive planation surfaces formed on rapidly uplifting anticlines in the foreland of the Tian Shan with a combination of field mapping, surveying, and analysis of digital elevation models (DEMs). We exploit optically stimulated luminescence (OSL) dating and cosmogenic radionuclide (CRN) dating to establish average rock-uplift rates of these active folds over the past 80 kyr and to show that striking changes in the rates of lateral bedrock erosion on kiloyear timescales must be invoked to explain the presence of extensive planation surfaces—surfaces now abandoned and dissected by narrow canyons. Finally, we discuss the extent to which these changes could occur as a result of modest shifts in the balance between sediment and water flux and/or changes in the flood frequency.

2. Valley Widening, Lateral Planation, and the Formation of Strath Terraces

2.1. Controls on the Ratio of Lateral and Vertical Erosion Rates

Bedrock-valley width and the formation of strath terraces are fundamentally controlled by the ratio of lateral erosion to vertical incision of streams. Herein, the terms "incision," "vertical incision," or "vertical erosion" are used to describe the downward cutting of a river into its bed and the removal of underlying bedrock. "Lateral erosion" and "horizontal erosion" are used to describe any erosion process that acts in a (sub)horizontal

direction. Finally, the terms "planation," "lateral planation," "beveling," and "lateral beveling" describe the fluvial cutting of a (sub)horizontal, approximately planar surface. Lateral bedrock planation occurs during episodes when lateral erosion rates are high compared to incision rates. In turn, during times when river incision dominates, planation surfaces are incised, strath terraces form, and valleys narrow (Gilbert, 1877; Hancock & Anderson, 2002; Merritts et al., 1994; Pazzaglia, 2013). We note here that most studies of extensive strath terrace formation have been performed in landscapes with weakly consolidated lithologies (Allen et al., 2013; Brocard & van der Beek, 2006; Collins et al., 2016; Cook et al., 2014; Fuller et al., 2009; Hancock et al., 1999; Langston et al., 2015; Lavé & Avouac, 2001; Molnar et al., 1994; Montgomery, 2004; Schanz & Montgomery, 2016) and that the width of planation surfaces has been linked to the strength of bedrock (Allen et al., 2013; Brocard & van der Beek, 2006; Montgomery, 2004; Römer, 2010; Schanz & Montgomery, 2016). However, strath terraces also form in resistant lithologies, such as granites and quartzite (Burbank et al., 1996; Pratt-Sitaula et al., 2004).

Results from physical experiments and stream power theory suggest that both lateral and vertical erosion rates are strongly controlled by the link between sediment flux to a stream and the transport capacity of the river (Hancock & Anderson, 2002; Johnson & Whipple, 2007; Langston et al., 2015; Schumm, 1969; Sklar & Dietrich, 2001, 2004; Turowski et al., 2008, 2007). Within a river channel, erosion of bedrock primarily occurs by impacts of bedload particles against the channel bed and against the channel walls (Johnson & Whipple, 2010; Sklar & Dietrich, 2001, 2004). If the transport capacity is high enough to mobilize all sediment supplied to the channel, bedload transport is concentrated near the channel thalweg, thereby allowing for efficient incision of the channel bed and simultaneously limiting the rate of channel wall erosion (Hartshorn et al., 2002; Johnson & Whipple, 2010; Shepherd, 1972; Turowski et al., 2008). In the end-member case where channel incision strongly dominates, a single, narrow canyon is formed. In contrast, where sediment flux from upstream or from hillslopes adjacent to a stream overwhelms the transport capacity of the river, such that the downstream gradient of sediment flux is negative, sediment is deposited and shields (part of) the channel bed from incision (Johnson & Whipple, 2010; Sklar & Dietrich, 2001, 2004). In addition, the presence of such bed cover is expected to increase the frequency of bedload transport near the channel walls and, therefore, enhance the absolute rate of lateral erosion within a channel (Beer et al., 2017; Hartshorn et al., 2002; Johnson & Whipple, 2010; Shepherd, 1972; Turowski et al., 2008). Similarly, high lateral erosion rates have been linked to the presence of channel roughness (Fuller et al., 2016). These processes point to a potentially complex interaction of lateral and vertical erosion on the channel scale in response to changes in the ratio of transport capacity and sediment flux.

Where some lateral erosion occurs (with or without vertical incision), wide bedrock valleys can form. Their widening rates are limited by the frequency at which channels impinge on valley walls and should therefore, to first order, inversely scale with valley width (Brocard & van der Beek, 2006; Cook et al., 2014; Hancock & Anderson, 2002). In addition, the height of channel walls likely controls the rate of valley widening (Malatesta et al., 2016). As a consequence, valley width across an active uplift should be controlled by a competition between the rate of river incision (that acts to increase valley wall height) and the rate at which rivers rework the active valley surface (the lateral channel mobility). This relationship has been experimentally demonstrated for unconsolidated sediment but is hypothesized to also hold at least for weak bedrock (Bufe et al., 2016). In turn, the lateral mobility of alluvial channels has been linked to the ratio of transport capacity to sediment flux (Bufe et al., 2016; Constantine et al., 2014; Wickert et al., 2013), as well as to changes in the boundary conditions, such as the confinement of the flow (Bufe et al., 2016).

In summary, changes in the ratio of transport capacity to sediment flux can have three effects. First, an increased sediment load or decreased transport capacity can shift the ratio of sediment flux to transport capacity to greater than one and lead to a negative downstream gradient in sediment transport rates. The resulting aggradation shields the channel bed, thereby decreasing vertical incision rates (Hancock & Anderson, 2002; Johnson & Whipple, 2007; Langston et al., 2015; Sklar & Dietrich, 2001, 2004; Turowski et al., 2007). Second, such increases in bed cover and/or roughness can enhance the frequency of impacts on channel walls and promote valley widening (Beer et al., 2017; Fuller et al., 2016; Hartshorn et al., 2002; Shepherd, 1972; Turowski et al., 2008). Third, an increased sediment flux typically increases the lateral mobility of alluvial rivers (Bufe et al., 2016; Constantine et al., 2014; Wickert et al., 2013) and thus augments the rate of valley widening due to the enhanced frequency and/or persistence of contact between a river and the walls that bound it (Bufe et al., 2016).

Changes in the ratio of transport capacity to sediment flux have commonly been linked to external forcings, such as to climatically controlled increases in sediment fluxes (Bookhagen et al., 2006; Bull, 1990; DeVecchio et al., 2012; Dey et al., 2016; Formento-Trigilio et al., 2003; Fuller et al., 2009; Hancock & Anderson, 2002; Jansen et al., 2011; Molnar et al., 1994; Pan et al., 2003; Pazzaglia & Brandon, 2001; Wegmann & Pazzaglia, 2002), changes in the water flux (Hanson et al., 2006), changes in vegetation density (Collins et al., 2016), or a combination of the above (Pratt-Sitaula et al., 2004; Schildgen et al., 2016). Other possible processes controlling stream power and, thus, transport capacity and rates of channel incision include downstream changes in base level due, for example, to sea level changes, downstream aggradation or degradation (Castillo et al., 2013; Finnegan & Balco, 2013; Merritts et al., 1994; Pazzaglia & Gardner, 1993), or changes in tectonic forcing (Cook et al., 2013; Grimaud et al., 2016; Yanites et al., 2010). In addition to external forcings, rapid changes in incision rates can happen autogenically such as in meandering bedrock rivers with autogenic bedrock-meander formation and cutoff (Finnegan & Dietrich, 2011). Similarly, bedrock terraces have been modeled to form in meandering rivers with a constant incision rate and autogenically varying lateral erosion rates (Limaye & Lamb, 2014, 2016).

Understanding the relative magnitudes of changes in vertical and lateral erosion rates has important implications for interpreting the timing and rate of strath formation, as well as the response of rivers to climatic changes. Several studies reveal the unsteadiness of lateral erosion rates and the complex link between lateral and vertical incision (Davis, 1902; Lavé & Avouac, 2001; Limaye & Lamb, 2016; Malatesta et al., 2016; Merritts et al., 1994; Pazzaglia, 2013; Pazzaglia & Gardner, 1993; Pazzaglia et al., 1998; Turowski et al., 2008; Wegmann & Pazzaglia, 2009). However, many strath-terrace formation models primarily focus on variations of vertical incision rates as a function of the degree of bed cover, whereas lateral erosion rates are either not considered or assumed to scale with bed shear stress and, therefore, to be independent of the sediment flux (DeVecchio et al., 2012; Fuller et al., 2009; Gilbert, 1877; Hancock & Anderson, 2002; Langston et al., 2015; Merritts et al., 1994; Molnar et al., 1994; Pan et al., 2003; Zaprowski et al., 2001). Whereas decreases in valley-widening rates with increasing valley width can be modeled (Brocard & van der Beek, 2006; Hancock & Anderson, 2002), the significance of changes in lateral erosion rates due, for example, to variations in the frequency of sediment impacts on the channel wall (Fuller et al., 2016; Hartshorn et al., 2002; Shepherd, 1972; Turowski et al., 2008), changes in the angle between the eroding channel and the eroded wall (Cook et al., 2014), or changes in the lateral mobility of channels (Bufe et al., 2016; Constantine et al., 2014; Wickert et al., 2013), remains unclear. Here we address this knowledge gap by documenting changes in lateral erosion rates during the planation of actively uplifting folds in the foreland of the Tian Shan.

2.2. Calculation of Lateral Erosion Rates

Simple spatiotemporal arguments are used to constrain changes in average lateral and vertical bedrock erosion across actively uplifting folds in the foreland of the Tian Shan. As discussed above, these rates respond partly to the same external controls. Here we treat them first as independent variables and then discuss their interactions. Given the plan view area of a river valley (A_i) created during an episode dominated by channel incision with some duration (Δt_i), an average areal planation rate within the valley (P_i) can be estimated as follows:

$$P_i = \frac{A_i}{\Delta t_i}. \tag{1}$$

(Figure 2). For the fluvial planation of a surface with area (A_b) that is beveled during a time interval dominated by lateral erosion (Δt_b), an equivalent areal planation rate (P_b) can be obtained:

$$P_b = \frac{A_b}{\Delta t_b}. \tag{2}$$

(Figure 2). Equations (1) and (2) yield average planation rates across duration Δt and do not account for effects such as the frequency of contacts between the channel and the valley walls (Brocard & van der Beek, 2006; Hancock & Anderson, 2002) or for variations in rates on timescales shorter than Δt_i and Δt_b. Nonetheless, because this caveat applies to both valley- and strath-planation rates derived from equations (1) and (2), these estimates provide a useful comparison between planation rates during incision versus beveling episodes. Note that the rates P_i and P_b are defined only for the area that is eroded by lateral planation of

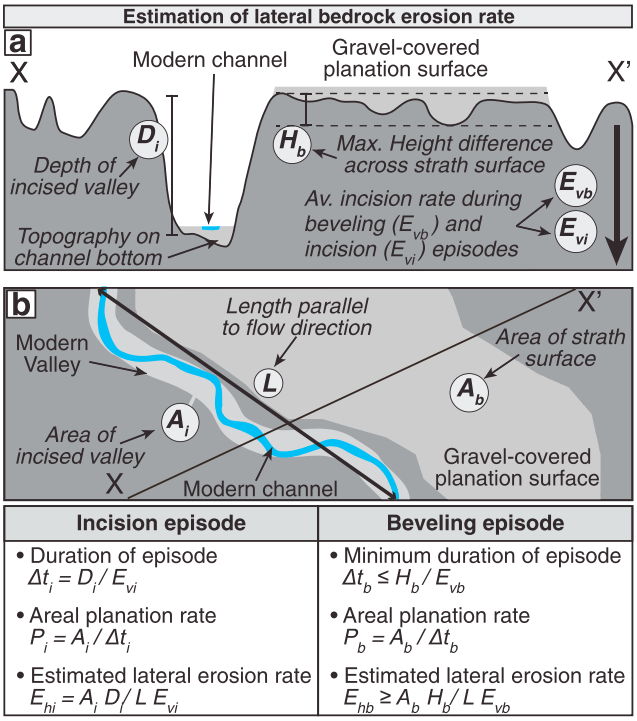

Incision episode	Beveling episode
• Duration of episode $\Delta t_i = D_i / E_{vi}$	• Minimum duration of episode $\Delta t_b \leq H_b / E_{vb}$
• Areal planation rate $P_i = A_i / \Delta t_i$	• Areal planation rate $P_b = A_b / \Delta t_b$
• Estimated lateral erosion rate $E_{hi} = A_i\ D / L\ E_{vi}$	• Estimated lateral erosion rate $E_{hb} \geq A_b\ H_b / L\ E_{vb}$

Figure 2. Conceptual sketch showing the calculation of lateral and their controls on rates during an episode of planation with minimum duration of Δt_b and an episode of incision with duration Δt_i (a) Cross section across incised fold shown in Figure 2b. A river incising into an uplifting fold at a rate E_{vb} during a planation episode and E_{vi} during an incision episode is shown (these two incision rates can be different). The maximum height difference across the strath (H_b) and the depth of the canyon (D_i) can be used to calculate the duration of the beveling and incision episodes respectively. (b) Plan view of the fold showing the eroded areas created during the beveling (A_b) and the incision (A_i) episodes. These areas can be used to calculate areal planation rates (P_b and P_i). When normalized by a length scale parallel to the mean flow direction, calculated lateral erosion rates are equivalent to a single, straight river moving in one direction.

rivers. Therefore, the planation areas A_b and A_i do not include the area that is occupied by river channels and the area that is formed through hillslope erosion.

The duration of an incision episode (Δt_i) can be estimated as follows:

$$\Delta t_i = \frac{D_i}{E_{vi}}, \tag{3}$$

with D_i being the depth of the incised valley and E_{vi} an average vertical erosion rate calculated across the entire incision interval Δt_i (Figure 2). Commonly, equation (3) is used in a rearranged form to calculate the incision rate, E_{vi}, with constraints on the ages of landforms preserved within an incised valley (Hancock & Anderson, 2002; Lavé & Avouac, 2001; Molnar et al., 1994; Pazzaglia, 2013; Pazzaglia & Brandon, 2001).

For a lateral beveling episode, an analogous rate can be calculated from the maximum height difference across the entire strath surfaces, H_b, and an average vertical erosion rate during the beveling episode, E_{vb}. We assume that the height difference across the beveled surface is due to incision into the surface that occurs in concert with lateral planation. If there were no incision, the beveled surface would be flat (and the following equation would break down). Therefore, the fluvially eroded strath surface that is created by one or multiple channels incising at an average vertical erosion rate, E_{vb}, develops a maximum height difference, H_b, across the entire strath surfaces that depends on the incision rate and the time interval, Δt_b, within which each point on the strath surface is visited by eroding rivers:

$$\Delta t_b \leq \frac{H_b}{E_{vb}}. \tag{4}$$

In other words, lateral planation must happen at a rate higher than or equal to the time necessary to incise the height H_b that is equivalent to the topographic relief on the strath surface (Figure 2). In addition to height differences created by ongoing channel incision, some topography on a planation surface may reflect height variations on active channel beds or differences in elevation among channels within a multithreaded system. Therefore, the duration calculated with equation (4) is a maximum estimate. Importantly, the planation surface could be actively beveled for a duration longer than Δt_b, but each point on the planation surface has to be revisited within a time $\leq \Delta t_b$ by rivers incising at a vertical rate E_{vb} in order to maintain a maximum height difference across the entire surface of H_b.

Valley-width evolution and the formation of strath terraces are commonly studied on the scale of a single river that incises into bedrock and, where lateral erosion is significant, sweeps back and forth across a valley floor. We stress here that the above equations are independent of the number of streams that erode the valley. However, in addition, we can use the above areal planation rates to estimate rates of horizontal bedrock erosion (E_h) equivalent to a single straight river moving laterally in one direction: for the incision episode:

$$E_{hi} = \frac{A_i}{L\ \Delta t_i} = \frac{A_i E_{vi}}{L\ D_i} \tag{5}$$

and for the beveling episode:

$$E_{hb} = \frac{A_b}{L\ \Delta t_b} \geq \frac{A_i E_{vb}}{L\ H_b}, \tag{6}$$

with L being the length of the eroded surface in the average flow direction (Figure 2). These lateral bedrock erosion rates of a hypothetical, single, straight river do not correspond to real measurable bank erosion rates where channels are sinuous or planation surfaces are cut by multithreaded, braided streams. However, these

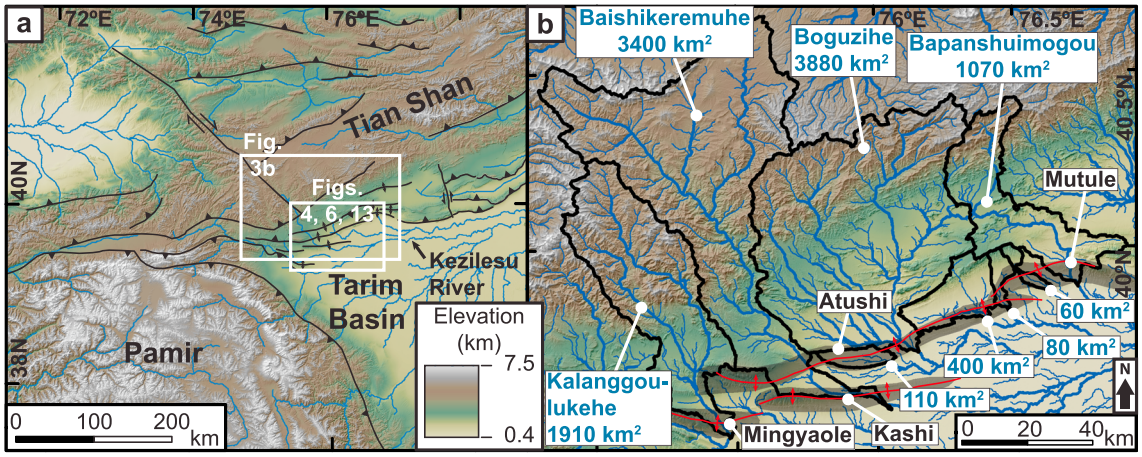

Figure 3. Topographic overview of the study area. (a) Inset showing the location of the study area and panels in Figures 4, 6, and 13. (b) Watersheds of rivers draining across the studied folds in the foreland of the Tian Shan. Folds are gray shaded; fold axes are red. Blue numbers denote catchment areas. Only major catchment names are given.

rates serve as an estimate for the order of magnitude of lateral bedrock erosion rates in the Tian Shan foreland, and they can be used to compare changes in planation rates between different time intervals. Moreover, they allow the comparison of planation rates on different sized folds and on folds that are experiencing contrasting rates of rock uplift.

3. Geological Setting

The Tian Shan is a major intracontinental mountain range, striking east-west from Tajikistan to northwest China (Figure 3). It formed by the collision and accretion of northward drifting island arcs in the Palaeozoic and Mesozoic (Bazhenov et al., 2003; Carroll et al., 1995) and the reactivation of old structures around 35–25 Ma due to the Indo-Asian collision (Abdrakhmatov et al., 1996; Bande et al., 2017; Coutand et al., 2002; Hendrix et al., 1992; Molnar & Tapponnier, 1975; Scharer et al., 2004; Sobel & Dumitru, 1997; Yin et al., 1998). Geodetic studies show that a total of 20–25 mm/yr of convergence between India and stable Eurasia is accommodated across the Tian Shan—a rate representing 40–60% of the total Indo-Eurasian convergence across this orogen (Abdrakhmatov et al., 1996; Zhang et al., 2004; Zubovich et al., 2016, 2010). In westernmost China, at the junction of the Tian Shan, the Tarim Basin, and the Pamir, deformation has stepped southward from the Tian Shan front that is cored by pre-Cenozoic rocks into the Cenozoic foreland over the last 25 Myr (Heermance et al., 2008; Jia et al., 2015). The most recent phase of this southward migration is the growth of three anticlines: the Kashi, Atushi, and Mutule anticlines (Figures 3 and 4) (Heermance et al., 2008; Jia et al., 2015). Other active folds to the west, notably the Mingyaole and Mushi anticline (Figure 4), are interpreted to be structures resulting directly from the collision between the Pamir and the Tian Shan (Li et al., 2012, 2013, 2015a, 2015b) and are not considered in this study. However, the erosion processes described here also affected parts of these structures.

The Kashi fold (Figure 4) extends east to west for ~60 km and is a doubly plunging detachment anticline with a tight, box-like shape and steeply dipping limbs. Kashi's elongate, tapered nose is propagating eastward into the Tarim Basin at rates of ~40 mm/yr (Chen et al., 2007; Scharer et al., 2004). An eastward decreasing cumulative uplift of $>$2.5 km across the fold (Figure 5a) and two paleomagnetic ages constrain average rock-uplift rates over the last 0.8–1.4 Myr to be 2.4 ± 0.5 mm/yr in the west and 1.4 ± 0.5 mm/yr in the east (Bufe et al., 2017; Chen et al., 2007; Scharer et al., 2004). The 100 km long and ~10 to 15 km wide Atushi anticline (Figure 4) is similarly interpreted as a rapidly eastward propagating, box-like, near-isoclinal detachment anticline with cumulative structural uplift in the west of ~4 km (Figure 5b) decreasing eastward to $<$2 km (Heermance et al., 2008; Scharer et al., 2006, 2004). Average rock-uplift rates since fold initiation are on the order of ~3.5 ± 0.8 mm/yr (Bufe et al., 2017; Heermance et al., 2008; Scharer et al., 2004). As the Atushi fold propagated eastward, it interfered with the westward propagating Mutule fold (Scharer et al., 2004) (Figure 4). The westernmost tip of the Mutule fold is interpreted as a detachment fold with a likely

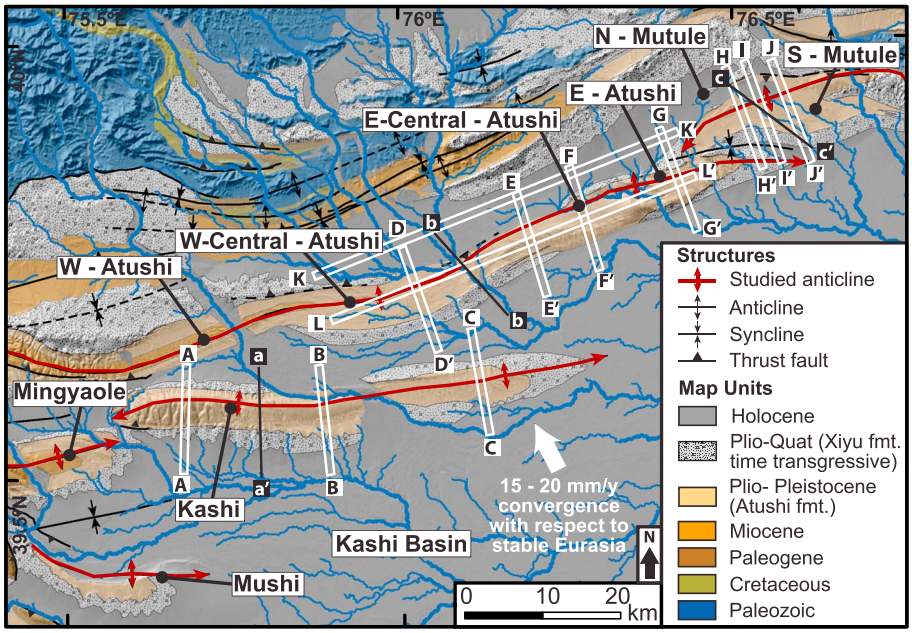

Figure 4. Simplified geologic map of the study area adapted from Heermance et al. (2007) and locations of profiles in Figures 5 and 10.

initiation age of 0.8–1 Ma and a cumulative uplift of <2 km (Scharer et al., 2004), implying average rock-uplift rates of ~2 mm/yr. About 10 km east of Mutule's western tip, total structural uplift rapidly increases to nearly 6 km (Figure 5c) implying uplift rates exceeding 4–5 mm/yr. Here a southward dipping thrust fault controls the uplift of the structure (Figures 4 and 5c).

Over 6 km of Tertiary strata fill the Kashi Basin and record sedimentation from the early Paleogene to today (Heermance et al., 2007). Early to mid-Paleogene marine sediments (including evaporites) are unconformably overlain by fluvial and lacustrine sandstones, siltstones, and shales of the Miocene Wuqia Group (Figure 4). The Plio-Pleistocene Atushi Formation conformably overlies the Wuqia Group and consists of mostly low-energy fluvial sediments composed of weakly to moderately cemented sandstone, siltstone, and mudstone with uncommon pebble conglomerates (Figure 4). The cores of the Atushi, Kashi, and Mutule anticlines all expose this easily erodible Atushi Formation and only in the westernmost part of the Atushi fold are older units exposed (Figure 4). Throughout the western Tarim Basin, the time-transgressive, moderately cemented, pebble-to-boulder conglomerate of the Xiyu Formation overlies the Tertiary strata (Charreau et al., 2009) (Figure 4). The unit has varying stratigraphic thickness, is laterally discontinuous, and youngs basinward, thus recording the southward advance of both the deformation and the gravel front over the last 25 Myr (Heermance et al., 2007).

All folds in the foreland are crossed by braided, commonly ephemeral rivers with a coarse bedload (pebble to cobbles with a small boulder fraction) and also a high suspended sediment load. In between the folds, large alluvial fans have been built by streams emerging from the Tian Shan mountain front to the north (Figures 3 and 4). Catchment areas of antecedent streams vary more than 50-fold, ranging from <80 km^2 to nearly 4,000 km^2 (Figure 3), and their headwater geomorphology shows that the catchments have been largely unglaciated (Stroeven et al., 2013). Notably, the western Mutule fold is crossed by relatively small streams (typical catchment areas of 50–80 km^2) draining the faulted ridge to the north of the fold, whereas antecedent drainages of the Atushi and Kashi folds comprise large catchment areas (Figure 3). All streams of the smaller (<1,000 km^2) catchments are currently ephemeral, but even the largest drainages have a highly variable streamflow with only small discharges outside the snowmelt season and between major thunderstorms. The northwestern Tarim Basin (Figure 3) is characterized by an arid desert climate (<70 mm/yr precipitation), such that the major rivers are fed by meltwater from the high peaks of the Tian Shan, whereas cloudbursts drive ephemeral discharge on many alluvial fan systems. However, at least five, several kiloyear-long episodes with a wetter climate have been reported within the past 40 kyr (Yang & Scuderi, 2010; Yang et al., 2008).

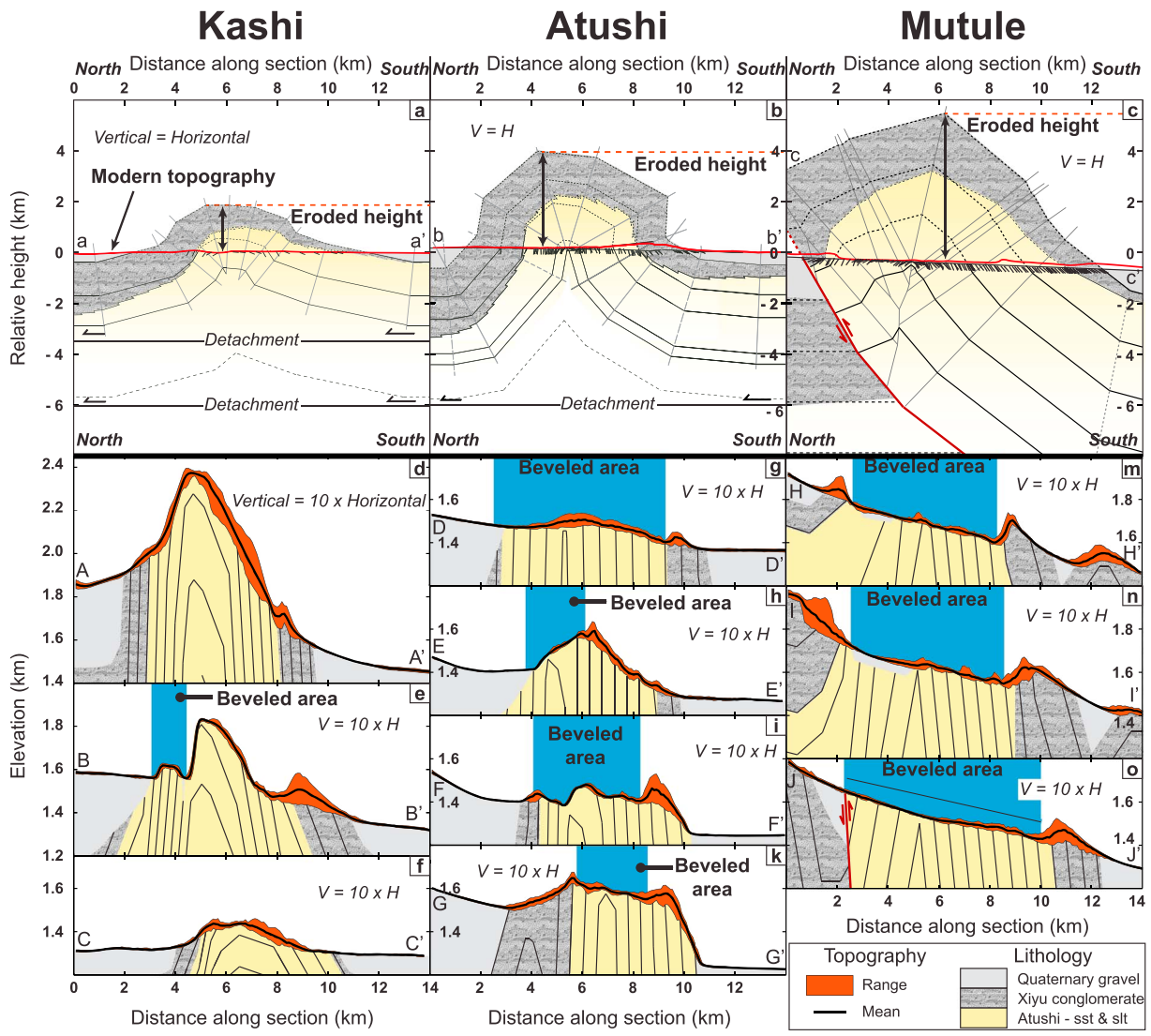

Figure 5. Profiles across three folds in the study area. See Figure 4 for profile locations. (a–c) Structure profiles (no vertical exaggeration) from field mapping and analysis of seismic sections. Figures 5a and 5b are adapted from Scharer et al. (2006), and Figure 5c is from mapping by the authors (Figure S1). (d–o) Swath profiles (1 km wide) across Kashi, Atushi, and Mutule folds approximately perpendicular to the fold axes with tenfold vertical exaggeration. The underlying lithology (colors), the bedding (black lines), and fold hinges separating dip domains (gray lines—only in Figures 5a–5c) are sketched from mapping by the authors and published structural sections and maps (Heermance et al., 2007; Scharer et al., 2006). Beveled surfaces (some now deformed) are marked by blue bands.

The base level evolution in the Tarim Basin is poorly known. Rapid foreland sediment accumulation rates of 0.3–0.8 mm/yr have been documented for sediments deposited between 0.8 and 3.4 Ma (Chen et al., 2007; Heermance et al., 2007). Given some isostatic compensation, such rates could imply that the foreland basin has been rising at rates of ~0.1–0.3 mm/yr through the Quaternary. However, loading and flexure of the Tarim Basin likely reduces the base level change due to aggradation. Clearly, the rates of aggradation are lower than the uplift rates of most of each fold's length, but some structures, such as the easternmost Kashi fold, are buried beneath the alluvial plain (Chen et al., 2002, 2007). Little evidence exists for major lakes just south of the Kashi and Atushi folds that might have caused rapid changes in the base level.

4. Methods

4.1. Mapping and Sedimentology

Topographic analysis and terrace mapping was done using both the 90 m Shuttle Radar Topography Mission version 4.1 (SRTMv 4.1) DEM (Jarvis et al., 2008) and satellite imagery in Google Earth® followed by ground

truthing and descriptions of the sedimentary terrace cover in the field. In order to determine the nature of the approximately planar erosion surfaces and to obtain constraints on the timing and rates of incision and lateral erosion, fluvial gravel deposits covering parts of the fold areas were characterized, mapped, and dated. These sediments were manually outlined on satellite imagery, and elevations of gravel-covered terrace treads and rivers were estimated using the SRTM DEM with nominal uncertainties of ~5–10 m (Gorokhovich & Voustianiouk, 2006; Rodríguez et al., 2006). In addition, the river crossing the Mutule fold, as well as line transects on the top of selected gravel-covered terraces on Mutule and Kashi, were surveyed using a Trimble Geo-XH differential GPS, yielding relative elevations with uncertainties of <1 m. Instead of using the DEM elevations, these GPS measurements (where available) were used to estimate the vertical separation between terrace treads and the modern river (see Text S1 in the supporting information). On the basis of terrace and river elevations, distinct terrace levels were identified. Thicknesses of strath-covering sediments on central Atushi and central Mutule were evaluated by measuring the vertical separation between the gravel top and the bedrock-cover interface, that is, strath surface, using a laser rangefinder along gullies that clearly expose the strath. Given some surface modification by deflation, inflation, and surface erosion, we identified largely unmodified gravel surfaces from their restricted surface topography and the presence of desert pavement. Uncertainties in the thickness estimates from measurement errors range between ±0.3 and ±0.7 m and were assessed by repeat measurements.

Clast imbrications ($n > 650$) in 14 locations were measured based on multiple exposure surfaces with diverse orientations and depth beneath the gravel cover surface in order to limit the bias related to oversampling of a particular orientation. Clast orientation and depth below the terrace surface were recorded with a compass and a laser rangefinder, respectively. Changes in source areas between the terrace gravels and the modern river channels were assessed using lithologic clast counts along nine surface transects in modern river beds and four depth transects on exposures of fluvial terraces. In a separate suite of measurements on the central Mutule fold, we measured clast sizes along three surface transects in modern river beds and seven depth transects on fluvial gravel outcrops (Wolman, 1954). The mapped distribution of gravel deposits, their elevations, thicknesses, and their sedimentology, as well as the composition and imbrication directions of individual clasts, were used to interpret the provenance of clasts and the depositional environment of each deposit. See Texts S2 and S3 for additional details.

4.2. Optically Stimulated Luminescence (OSL) Dating

Thirteen sand lenses within gravelly deposits that cover bedrock straths were sampled for OSL dating on the three upper terraces of the Mutule fold, at two locations on the western and eastern Atushi fold, as well as on the highest terrace on the Kashi fold. The samples were processed and measured in the Laboratory of Luminescence Research at the Institute of Geology, China Earthquake Administration, Beijing, following standard techniques and a single-aliquot regenerative dose protocol (Murray & Wintle, 2000; Wintle & Murray, 2006). Dose rates were estimated by measuring activities of ^{238}U, ^{226}Ra, ^{228}Ra, ^{228}Th, and ^{40}K in sediment collected within a 15 cm radius around the OSL sample. We note that samples CK-1 and WCA-3 have exceptionally high U-series disequilibria, and their ages are reported, but not used in the analysis. The distribution of measured equivalent dose (D_e) values for the aliquots of each sample was modeled using a three-parameter minimum age model (MAM) (Galbraith & Roberts, 2012; Galbraith et al., 1999) and a central age model (CAM) (Galbraith & Roberts, 2012; Galbraith et al., 1999). We calculated the skew, kurtosis, and overdispersion and used the criteria by Arnold et al. (2007) to choose the most appropriate age model. Finally, we doubled the standard errors from the MAM and CAM models to obtain ages at the 2σ confidence level. These samples constrain the burial age of the dated lenses (the last time that the sand was transported). Therefore, they provide a minimum age estimate for the creation of the underlying strath surfaces and a maximum estimate for the time of terrace abandonment. See Texts S5 and S6 for more details on the methodology (Olley et al., 1996, 1997; Prescott & Hutton, 1988, 1994; Zander et al., 2007).

4.3. Cosmogenic Nuclide Dating

On the highest, most extensive Atushi terrace, eight samples were collected from a 3 m deep profile for ^{10}Be cosmogenic radionuclide (CRN) dating using established methodologies (Anderson et al., 1996; Hancock et al., 1999; Repka et al., 1997). The site lies ~60 m away from the terrace edge, with (micro)surface topography of <20 cm within a radius of several meters, and with a weakly developed desert pavement. Seven sand samples were collected from stratigraphic intervals each less than 10 cm thick and spaced 30–100 cm apart,

Table 1
Planation Surfaces and Depth of Incision of Folds in the Foreland of the Tian Shan

Fold	Depth of incision into highest beveled surface (m)[a]	Approximate total area of fold (km^2)[b]	Total beveled area (km^2)[b]	Percent beveled area	Area covered by incised (Late Quaternary) alluvium (km^2)[c]	Area covered by unincised (Holocene) alluvium (km^2)[c]	Percent of beveled area covered by alluvium
Mushi	30–60	300	84	28	29	43	86
Mingyaole	70–250	220	58	26	11	0	19
Kashi	50–90	460	84	18	36	45	96
West Atushi	30–70	120	53	44	0	0	0
West central Atushi	25–90	220	165	75	12	15	16
East central Atushi	80–120	150	71	48	0	11	16
East Atushi	200–280	70	21	31	0	0	0
North Mutule	0–10	40	37	91	11	21	87
South Mutule	10–50	180	92	51	10	2	13
Sum of all folds	NA	1,760	665	38	109	137	37

Note. NA, not applicable.
[a]Estimated from profiles on a 90 m SRTM. [b]Estimated using Google Earth ®imagery. [c]Fluvial deposits mapped using Google Earth ®imagery and ground truthed in the field.

and one sample consisting of 1 to 4 cm diameter quartz clasts was collected on the terrace surface within 3 m of the depth profile site. The samples were processed at the cosmogenic nuclide preparation laboratory at UC Santa Barbara following standard procedures (Bookhagen & Strecker, 2012), measured at the Purdue Rare Isotope Measurement (PRIME) Laboratory, and analyzed using a Monte Carlo depth profile simulator (Hidy et al., 2010) and the CRONUS-Earth-2008-v2.3 exposure age calculator (Balco et al., 2008). See Text S7 for more details on the methodology (Borchers et al., 2016; Chmeleff et al., 2010; Korschinek et al., 2010; Lal, 1991; Lifton et al., 2014; Nathan, 2010; Nelson et al., 2015; Nishiizumi et al., 2007; Stone, 2000). These samples constrain the abandonment age of the gravel deposit and also provide a minimum estimate for the age of the underlying strath surface.

5. Results

5.1. Planation Surfaces in the Foreland of the Tian Shan

The Kashi, Atushi, and Mutule folds have uplifted 2–5 km of rock over the past 1–2 Myr (Figures 5a–5c) (Chen et al., 2007; Heermance et al., 2008; Scharer et al., 2004). Despite this large cumulative uplift, the present-day surfaces of these folds lie only 100–800 m above the surrounding alluvial fans, thereby attesting to efficient fluvial and hillslope erosion that approximately matches rock-uplift rates (Figure 5). All three folds (Kashi, Atushi, and Mutule) expose a variably thick, outer rim of more resistant Xiyu conglomerates (Pliocene-Quaternary in age) that surround a core of weakly cemented, quite readily eroded sand and siltstones of the Plio-Pleistocene Atushi Formation (Figures 4 and 5). These rims of Xiyu conglomerates commonly stand above the Atushi Formation and attest to their slightly greater resistance to erosion (Figure 5). On Kashi and parts of Atushi folds, steep hillslopes ($>$5–10°) with deep gullies form a convex-up topography that is expected for actively growing anticlines eroded by efficient hillslope and gullying processes (Figures 5d–5f and 5h). However, in addition to steep limbs, strikingly extensive areas with mean slopes $<$5°, where relief within a radius of 1 km is $<$100–200 m, cover 20–90% of the studied structures (Table 1 and Figure 6). On these areas, steeply inclined beds of the folds (Scharer et al., 2004) are clearly visible both on satellite imagery (Figure 7) and in the field (Figure 8) and attest to the erosional nature of these nearly planar topographic surfaces that truncate the underlying beds. Even the fairly well consolidated Xiyu conglomerate is commonly planed off (Figures 5e, 5g, and 5h). The planar surfaces are clearly flatter than the steep, gullied limbs of, for example, western Kashi and many other active and inactive structures surrounding the studied folds (Figures 5d–5f and 6). Moreover, the planar surfaces can be preserved tens to hundreds of meters above local base level with steep fold limbs on either side (Figures 5e, 5g–5k, and 6). The contrast between planar and convex erosional topographies that occurs along structures with a uniform lithology, as well as the clear topographic scarps and the boundaries between erosional surfaces that crosscut the strike of the folds (e.g., Figure 7), suggests that erosional processes vary across the studied structures. Whereas hillslope

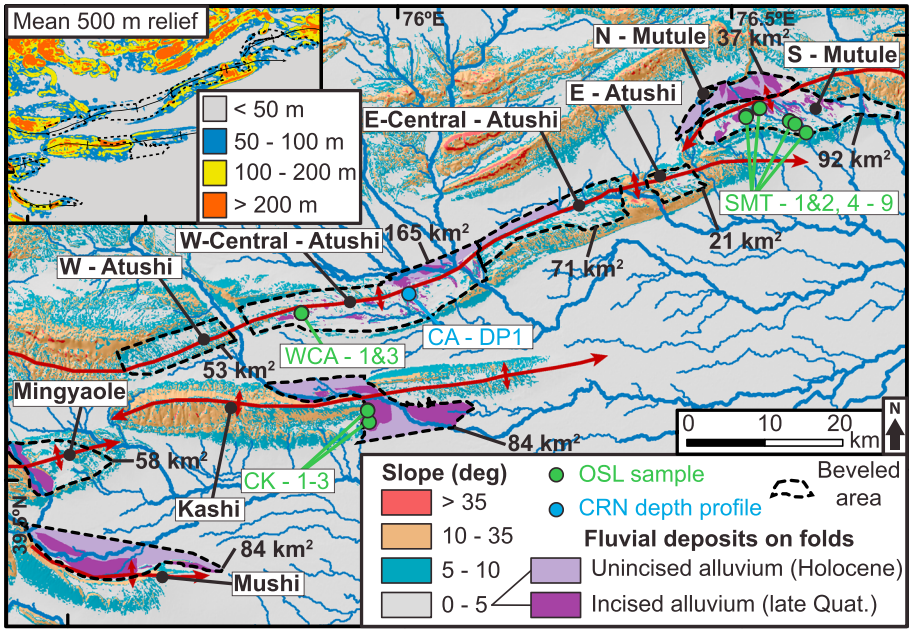

Figure 6. Mean slope and 500 m radius relief across the study area calculated with the 90 m SRTM DEM. Extent of beveling (in km^2) is based on the slope and topography of the surfaces across the folds. This extent and the distribution of Pleistocene and Holocene fluvial gravels across the folds were mapped on Google Earth® imagery and in the field. Upper surfaces of fluvial gravels have slopes ≪5°, except where terrace risers or flexural-slip scarps disrupt the surface. Green and blue dots mark the location of optically stimulated luminescence (OSL) and cosmogenic radionuclide (CRN) samples; red lines mark axes of anticlines. Holocene (light purple) and Pleistocene (dark purple) gravels with slopes <5° are shown on the folds. Other than on the folds, low-slope areas are largely formed by Holocene alluvial fans.

erosion and gullying within the Atushi sandstones and the Xiyu conglomerates (Figure 4) form steep (>5–10°) hillslopes, the wide planar platforms with slopes <5° are interpreted to have been eroded dominantly by the lateral planation of rivers. This interpretation is substantiated by the preservation of fluvial gravels covering parts of the beveled surfaces (Figures 6–8) as well as scattered remains of gravels where the fluvial cover has subsequently been eroded. Hereafter, these planar surfaces will be termed "beveled" or "planated" surfaces or areas.

Most beveled areas are currently incised 10 to >200 m by major antecedent streams and smaller consequent streams, forming strath terraces. The strath surfaces are well preserved where they are covered by fluvial gravel (Figures 6–8 and Table 1). In contrast, where thick, fluvial gravels are absent, a gently undulating topography of hills and gullies is common (Figures 8a and S3b) and the original strath surface at the time of fluvial planation is difficult to precisely reconstruct. Many of the strath terraces have been progressively tilted on the fold limbs, thereby recording continued uplift by the folds (Heermance et al., 2008; Scharer et al., 2006) (Figures 9a and 9c). Importantly, the alluvial fans upstream and downstream of the folds are largely unincised: a condition implying that the incision occurs in response to fold uplift with rates higher than the aggradation rates of the surrounding basins. Despite similar bedrock lithologies and local climate, a detailed consideration of each structure reveals that not all folds exhibit a similar distribution of beveled areas.

5.1.1. Beveling of the Kashi Fold

The western Kashi fold initiated 1.4 ± 0.3 Myr ago (Heermance et al., 2008) and has a typical convex-up topography with a steep, highly dissected, short northern limb, and a gentler sloping, dissected southern limb. These flanks bound a crest rising up to 800 m above the modern depositional plain (Figures 5d and 7b). The eastern part of the Kashi fold also shows an emergent fold nose (Figure 5f), but one that has seen more limited erosion (Scharer et al., 2004). This part of the fold is younger and is propagating eastward. Here folding began <1 Myr ago, and topographic emergence occurred much later than on the western tip of the fold (Chen et al., 2007). Both the western and the eastern parts have not experienced efficient beveling. Where the river Baishikeremuhe (Figure 3b) impinges obliquely onto the Kashi fold, it is deflected eastward down a

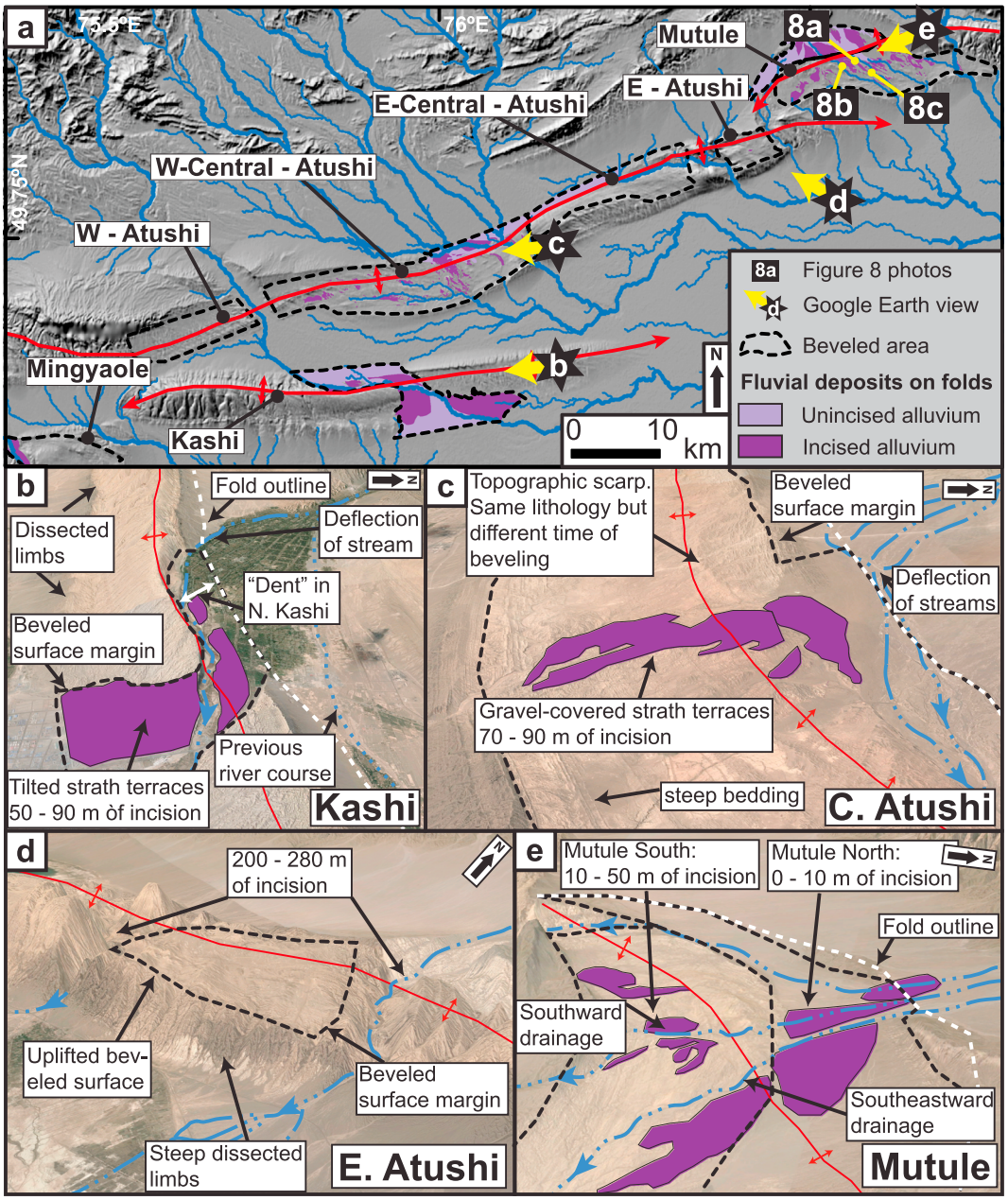

Figure 7. Google Earth® views of the three studied folds. (a) Hillshade map showing the locations of both Figures 7b–7e (black stars) and photos in Figure 8. Yellow arrows depict direction of view. Extent of beveling was mapped on Google Earth® imagery and in the field based on topography and slope. (b–e) Views of Kashi, Atushi, and Mutule. Black dotted lines mark beveled areas; blue dash-dotted lines approximate locations of modern rivers; purple areas depict major incised (Late Quaternary) gravels; red lines trace anticline axes and white dashed lines outline the folds (only in Figures 7b, 7c, and 7e).

topographic ramp that broadly parallels the fold flank (Figure 7b). Eventually, the Baishikeremuhe crosses the fold at an oblique angle of ~0–70°, but prior to being trapped in the current water gap, this river was deflected around the eastern nose of the fold (Chen et al., 2007). During times of active aggradation, the river may still flow around the fold's eastern nose, as suggested by well-preserved abandoned channels on the alluvial fan surface north of Kashi (Chen et al., 2007; Scharer et al., 2006). Where the modern river impinges onto the upstream flank of the fold, it has beveled a cusp-shaped indentation across the northern ~2 km of Kashi's northern limb (Figures 7b, 9a, and 9c). Downstream, on the southern limb of the

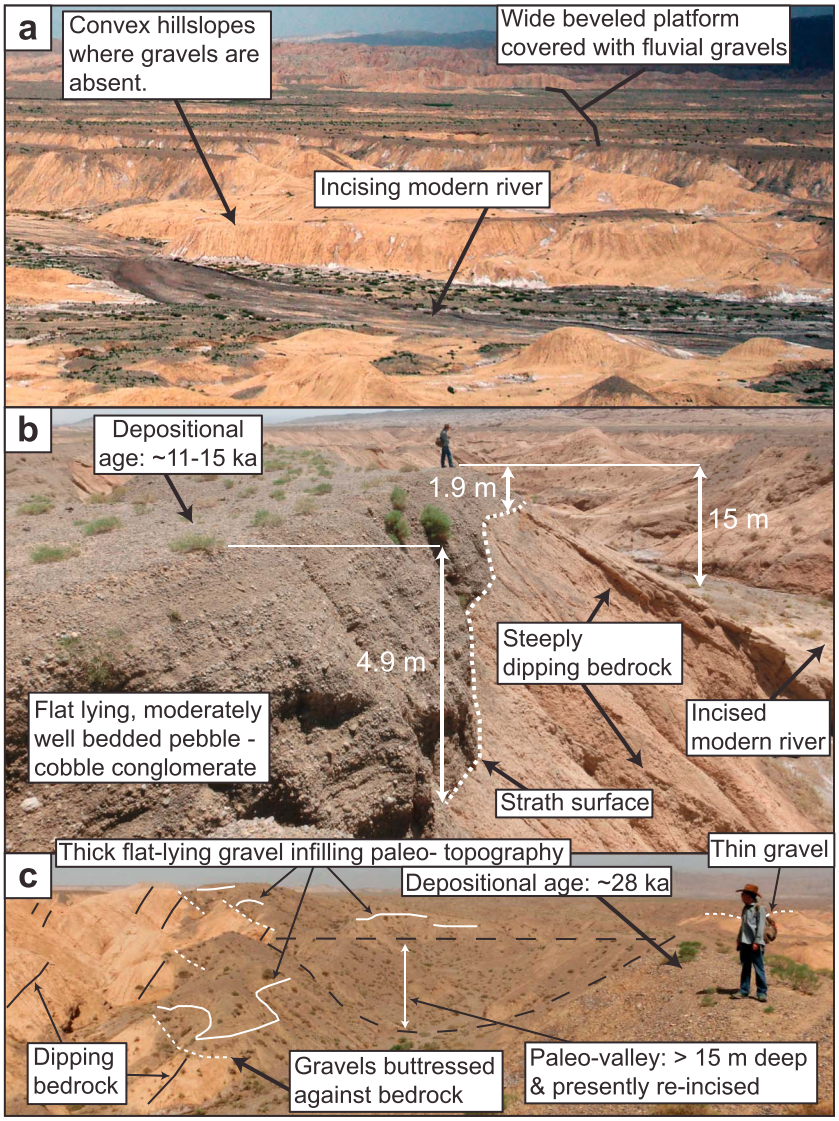

Figure 8. Field photographs of planation surfaces on Mutule. (a) Uplifted planation surfaces covered with fluvial deposits in the background and incising modern river in the foreground. Note the convex-up, steep hills that have been stripped bare of their fluvial cover. (b) Typical flat-lying gravel deposits with thicknesses of <1–6 m and meter-scale thickness changes. (c) Anomalously thick gravels buttressed against steeply dipping bedrock in paloevalley. See Figure 7 for photo locations.

fold, a series of eastward younging terraces document the progressive eastward migration of the river (Figures 9a and 9c) (Table 1).

5.1.2. Beveling of the Atushi Fold

In contrast to the Kashi fold, the west central part of the Atushi fold lacks a convex-up topographic profile, and instead forms a wide, planar platform with slopes commonly <5° and a mean 500 m radius relief of <50 to 100 m (Figures 5g, 6, and 7c). The WSW-ENE slope of ~0.7° along this 15 to 20 km long platform that both spans and trends parallel to the fold's axis is notably similar to the slope of a parallel topographic swath across the modern alluvial fans that impinge on the fold's upstream flank (Figure 10). This parallelism suggests that the west central Atushi fold has not been differentially tilted since its beveling. On the basis of localized, beveled "plateaus" of remnant incised topography, two extensively beveled areas, each ~10 km long and separated vertically by ~30–60 m, can be identified (Figure 10). The eastern surface is incised 70–90 m by the modern Boguzihe, whereas the preserved incision depth farther west is 25–45 m (Figure 10). Contrary to Atushi's western and central segments, the eastern part of the Atushi fold rises to a

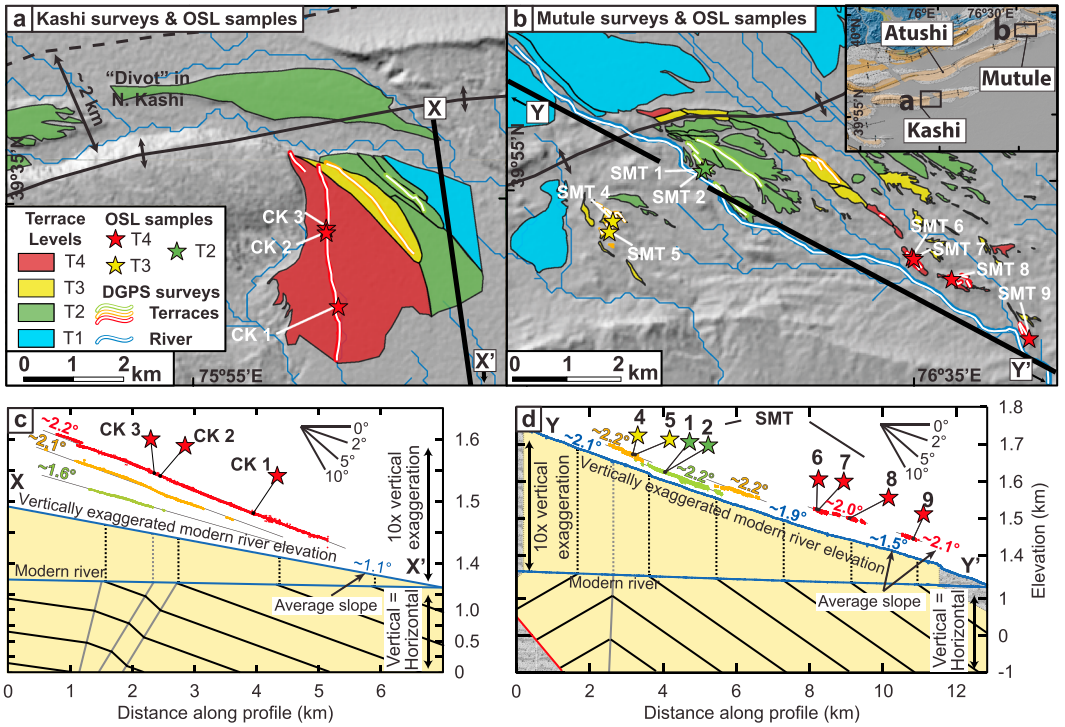

Figure 9. OSL sample locations, terrace surveys, and slopes on central Kashi and southern Mutule. (a) Map view of central Kashi anticline showing gravel cover of strath terraces mapped using Google Earth® and field mapping. Differential GPS surveys on terraces are shown as bold lines. (b) Map view of southern Mutule anticline. Differential GPS (DGPS) surveys on terraces and on the modern river are shown as bold lines. (c) Cross section across southern central Kashi. All GPS surveys and OSL sample locations (marked with stars) were projected onto the cross section X–X′. Structures are simplified from cross section of Figure 4a. Modern river profile is based on the 90 m DEM. (d) Cross section across southern Mutule. River profile from DGPS survey. Structures simplified are from Figure 4c.

height of >200 m with respect to the flanking basin (Figures 5h–5k). Here incision by antecedent rivers forms canyons, tens to hundreds of meters deep, and the limbs of the folds are steep and highly dissected by gullies (Table 1 and Figure 7d), similar to the flanks of the western Kashi fold (Figure 7b). Nonetheless, despite this surface uplift, two prominent, planar areas (totaling ~20 km^2) are preserved on the eastern Atushi fold (Figures 5i–5k and 7d).

5.1.3. Beveling of the Mutule Fold

Farther east, the Mutule fold has the most extensive low-lying beveled surface in the study area (Figures 5m–5o). In fact, the northern limb of the fold (~30% of the total fold width) is nearly completely covered with modern alluvial fans with rare bedrock outcrops beneath a slightly raised strath terrace that shows <5–10 m of incision down to local base level (Table 1 and Figures 6 and 7e). Greater surface uplift of strath terraces or less efficient recent erosion of the southern limb of the Mutule fold has led to 10–50 m of incision by modern channels into the uplifting fold (Table 1 and Figures 7e, 9b, and 9d).

In summary, the three folds described here record erosional geometries ranging from steep limbs eroded by gullying and hillslope erosion to aerially extensive, beveled surfaces that are preserved at heights ranging from 0 to 280 m above the modern rivers and are covered by varying amounts of fluvial sediment (Table 1). On the western central Atushi and the Mutule folds, between 50 and 90% of the folds are beveled with planation surfaces that lie <50–100 m above the current base level, whereas on eastern Atushi, the planation surfaces are raised to nearly 300 m and cover ~30% of the total fold area. On the Kashi fold, less than 20% of the fold has been planated and planation surfaces are preserved 50–90 m above the modern river (Table 1). Thus, striking spatial variations in the extent of planation occur across the Tian Shan foreland.

5.2. Fluvial Gravel Cover of Strath Terraces

Parts of the planar surfaces that are cut into the uplifting folds are covered by fluvial gravel that unconformably overlie the steeply bedded Atushi and Xiyu Formations (Figures 6–8). They present archives of fluvial

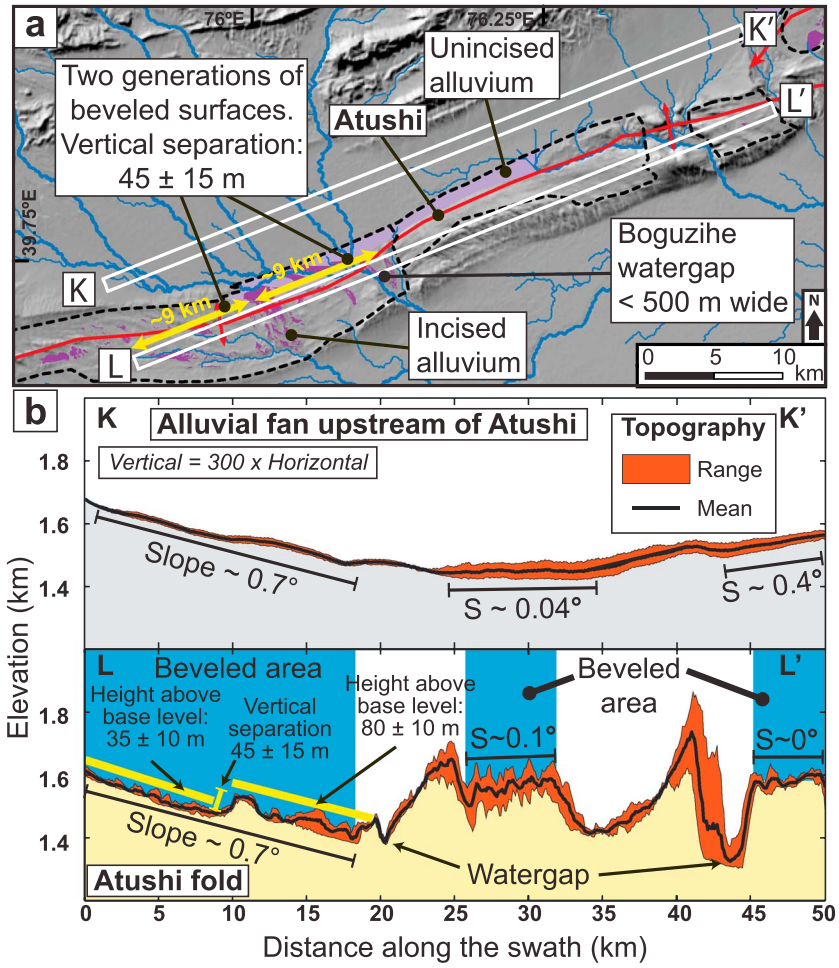

Figure 10. Comparison between the axis-parallel slope of the Atushi fold with that of the upstream alluvial fan. (a) Hillshade showing location of swath profiles K–K′ and L–L′ (cf. Figure 4 for regional context). Red lines mark fold axis. The extent of beveling was mapped on Google Earth® imagery and in the field based on topography and slope. (b) Swath profiles (1 km wide) approximately parallel to the Atushi fold axis along the fold and upstream alluvial fan. The color scheme for the sections as in Figure 5. Fold profiles show beveled surfaces at three different heights. Note that the axis-parallel slope (0.7°) of the beveled area on western central Atushi (0–19 km) parallels the slope of the upstream fan ~7 km to its north.

systems that existed at or shortly after the time of beveling. We mapped tread outlines of fluvial gravels where they are thick enough to be clearly visible on satellite imagery (Figure 6). With the exception of the Kashi and northern Mutule fold, the majority of the planation surfaces (>80%) do not preserve thick fluvial deposits (Table 1). Nonetheless, in these areas, scattered remnants of fluvial gravel that are too thin or too discontinuous to be visible in the satellite imagery can commonly be found in the field (Figures 8a and S3b).

The mapped deposits are assumed to cover an underlying strath surface and were grouped into terrace levels according to their height above the modern river. We did not attempt to correlate terrace levels between different folds. More than 90% of the planation surfaces on Kashi are covered with >5 m thick fluvial gravels. Four terrace levels separated by terrace risers can be distinguished, and their differential tilt records continued uplift of the Kashi fold (Figures 9a and 9c). On western central Atushi, only ~16% of the beveled area is covered by >0.5 m thick fluvial deposits. The highest of these deposits is ~80 m high, spans across the entire width of the fold (Table 1 and Figure 6), and is tilted across the northern and southern limbs of the structure (Figure 13 in Heermance et al., 2008). In contrast, no thick gravels were found on eastern Atushi (Figure 6). The fluvial gravels on Mutule are extensive in the north, but only 13% of the beveled surfaces on southern Mutule preserve >0.5 m thick fluvial gravels (Figures 9b and 9d and Table 1). These fluvial gravels on Mutule's southern limb reveal a somewhat complex geometry and correlating terraces across the several kilometer-wide

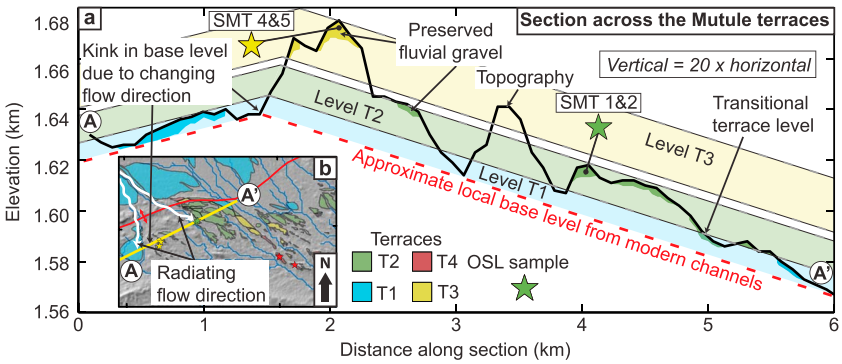

Figure 11. Map and topographic profile of the terraces on Mutule fold showing the large range of elevations at which terrace gravels are preserved. (a) Topographic cross section along the line marked in Figure 11b. Preserved fluvial gravels on straths are shown according to mapped terrace levels. Because the section is not perpendicular to the flow direction of rivers, the base level is not flat. On the basis of troughs in the topography, an approximate local base level is shown (dashed red line). Because the flow direction is changing across the section (cf. Figure 11b), the trend of the base level is, too, illustrating challenges in correlating fluvial gravels across the kilometer-wide surface of the Mutule fold. The transparent color bands mark the range of elevation across which gravel-covered strath terraces are preserved. (b) Map of the gravel-covered terraces on central Mutule (same as in Figures 9b and 9d) with preserved fluvial gravels. Radiating flow direction of rivers (white lines) are typical of alluvial fans.

fold poses a challenge, because the strath surface is not well preserved where gravels are absent and because antecedent rivers sweep from southward flow directions in the west to southeastward in the east (Figure 11). Therefore, the appropriate local base level is not always clear. Nevertheless, some well-preserved terrace risers are present, and four major terrace levels can be identified (Figures 9b, 9d, and 11). In contrast to the south tilted terraces on the Kashi fold (Figures 9a and 9c), the terraces on Mutule are inclined at slopes that are similar to the modern river and are not differentially tilted (Figures 9b and 9d).

5.2.1. Sedimentology

The gravels preserved on strath terraces are typically moderately sorted, granule-to-cobble conglomerates, with uncommon sand and silt lenses of up to 30–40 cm thickness, as well as rare boulders (Figures 8 and S2). Considerable grain-size variations between moderately to well-bedded horizons occur. Generally, beds are submeter thick and planar, but meter-scale channels and scours are common. Even within the thickest cover sequences, no clear evidence for major cut-and-fill events or hiatuses is apparent (with one exception: cf. Figure S3c). Clasts are typically subrounded to rounded (similar to the modern river) and imbricated, nonspherical clasts are abundant (Figures 8b and S2a). Note that in the case of the Mutule fold, despite the short travel distance ($<$10 km), clasts are still rounded because the catchment drains a ridge of Xiyu conglomerate (Figure 4) comprising rounded clasts. The deposits are matrix to clast supported with sandy or less commonly silty matrices. A mud fraction is present and drapes all grains, but thick deposits of clay to sand sizes only occur in uncommon lenses and pockets that likely represent slack-water deposits or minor channels (Figure S2a). On all folds, the surfaces of the fluvial cover sequences (the treads of gravel-covered terraces) are generally smooth with a visually estimated surface topography of $<$1 m (Figure 8). Undulations with amplitudes of tens of centimeters across several meters are interpreted as primary alluvial fan structures, whereas height differences of several meters typically occur only along terrace scarps or where flexural-slip scarps offset the strath surfaces, for example, Li et al. (2015b). Modifications to the primary topography of the gravel surfaces are observed where fines collect in deflation hollows and where relative coarsening of the surface occurs around small gullies (Figure S2c). We estimate visually that these surface modifications have magnitudes of $<$10 cm.

5.2.2. Terrace Cover Thickness

We mapped the thickness of two major deposits on the Atushi and Mutule folds (Figure 12). With respect to the planar preserved character of the abandoned, upper alluvial surface, we find that most of the cover sequences are between 1 and 6 m thick with uncommon deposits $>$10 m thick. In comparison to rather planar, upper gravel surfaces, the gravel thickness above a strath may vary by several meters across distances of a few meters, revealing a complex buried surface topography with meter-scale height differences (Figure 12). Some of the thickest flat-lying gravel deposits on Mutule are observed to buttress against steeply dipping

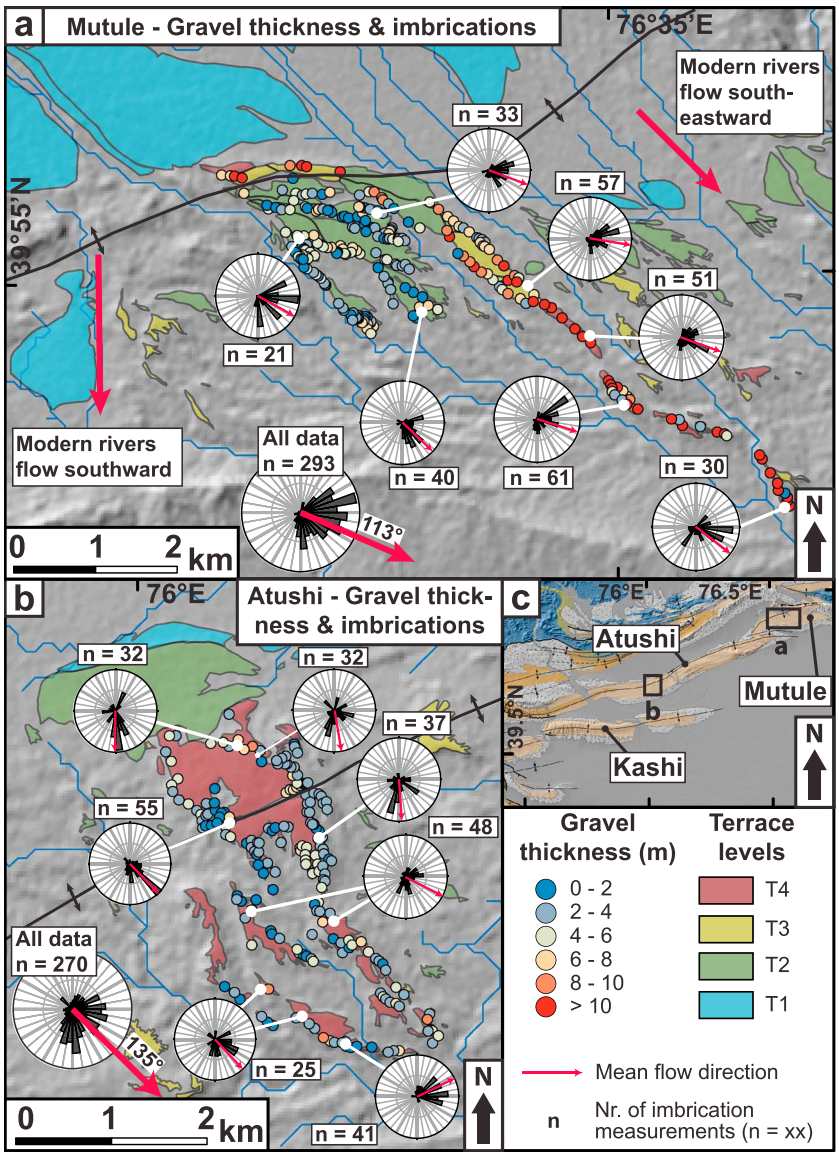

Figure 12. Imbrication direction and gravel thicknesses of fluvial deposits on major terrace sequences of (a) central Atushi and (b) southern Mutule. Notably, mean paleoflow directions approximate those of modern rivers. Gravel thickness is mostly <6 m, but some thicker deposits occur, especially along a narrow band on central Mutule. Because gravel surfaces are very planar with meter-scale relief of ≪1 m, abrupt changes in the gravel thickness at the meter scale indicate relief on the strath surface.

bedrock (Figures 8c and S3d). Where deposits are much thicker than a few meters, it is unlikely that they were mobilized in a single flood. They likely represent fill deposits that infill a previous topography. However, as already described, such thick deposits do not cover the majority of the uplifted planation surfaces on Atushi and southern Mutule. Instead, only thin, discontinuous remnants of fluvial gravels can be found (Figure S3). The gravel cover on the Kashi fold is much more continuous than on the Atushi and Mutule folds, and 2–6 m deep gullies do not reach the base of the gravels. Therefore, we did not systematically map gravel thicknesses on these deposits. However, our observations along the rims of the deposit suggest that gravel thicknesses are typically on the order of 4–10 m on the Kashi fold.

5.2.3. Imbrication Measurements

Imbrication measurements on gravel deposits of Atushi and Mutule show moderately dispersive flows consistent with a braided river system flowing on a gently inclined alluvial surface (Figure 12). On Mutule, the mean flow direction is ~113° from north, which is indistinguishable from the general flow direction of the

Table 2
Lithologic Clast Counts in the Study Area

Sample name (west to east)	Location	Latitude (°N)	Longitude (°E)	Elevation (m)	Number of counts	Noncarbonate rocks (%)	Total carbonate rocks (%)	Microcrystalline carbonate rocks (%)	Other carbonate rocks (%)
Bai1	River	39.7630	75.6106	1,924	119	57	43	9	34
Bai2	River	39.8690	75.5411	2,127	115	57	43	3	40
Bog3	River	39.8079	75.8146	1,854	130	25	75	28	46
Bog2	River	39.8871	75.9450	1,805	119	9	91	2	89
Bog1	River	39.8840	76.0563	1,605	117	17	83	15	68
CA_north	Terrace	39.7130	76.0111	1,480	111	30	70	9	61
CA_south	Terrace	39.7024	76.0233	1,458	125	26	74	10	64
EA_R1	River	39.8232	76.3541	1,337	125	5	95	67	28
MUT_R1	River	39.9410	76.4970	1,721	127	10	90	50	40
MUT_R2	River	39.9732	76.4986	1,910	124	8	92	41	51
SMT_north	Terrace	39.9207	76.5535	1,541	131	7	93	49	44
SMT_south_lower 4m	Terrace	39.8907	76.6080	1,380	141	12	88	56	32
SMT_south_upper 4m	Terrace	39.8909	76.6079	1,396	139	10	90	49	41
SMT_south_surface	Terrace	39.8909	76.6079	1,396	133	11	89	52	37
SMT_south_mean	Terrace	39.8909	76.6079	1,396	138	11	89	52	37
MUT_R3	River	39.9919	76.6927	1,453	119	14	86	31	55

modern river (Figure 12a). On Atushi, mean flow directions are generally southeastward, with a mean of ~135°, similar to the modern Boguzihe. Thus, in general, imbrications reveal a pattern of flow directions similar to the modern rivers.

5.2.4. Lithological Clast Counts

Based on catchment areas (Figure 3) and lithological clast counts (Table 2), three to five different source areas of streams crossing the folds in the study area can be defined (Figure 13 and Tables 2 and S2). In order to assess the similarity between clast distributions at two different sites, we calculated a similarity factor for each sample pair that is based on differences in the proportions of microcrystalline carbonate rocks and all other carbonate rock (Text S2 and Table S2). Sample pairs with values of $\leq$14% of this factor are considered similar (Text S2). Based on these data, it appears that the cover of the Mutule terraces has been deposited by local rivers draining the 60 km^2 catchment to their north (MUT R1 and R2—similarity factors of 1–18% between rivers and the Mutule terrace gravels with one outlier at 24%) rather than by the larger Bapanshuimogou River with a catchment of 1,070 km^2 on eastern Mutule (MUT R3—similarity factors of 21–28% between the river and the Mutule terrace gravels) (Figure 3). In turn, the pebbles on the Atushi fold are closest in composition to the largest and easternmost of the Boguzihe tributaries (Bog1—similarity factors 6–9%), whereas the other tributaries are more different (Bog 2 and 3—similarity factors 24–29%). Moreover, the Baishikeremuhe does not seem to have had a major influence in depositing the Atushi terrace cover (Bai 1 and 2—similarity factors 22–30%) (Figure 13). We conclude that efficient planation of folds that are being uplifted rapidly can occur by streams with catchment areas ranging from $<$100 km^2 to 4,000 km^2.

5.2.5. Clast-Size Counts

We measured clast sizes along three locations of a river crossing the Mutule fold, as well as seven terrace locations (Figure 14 and Table 3). The D_{50} and values of amalgamated terrace deposits are lower than those of the modern river, but both lie within 20% uncertainty bounds (2σ confidence level). Thus, in this location, a slight coarsening during times of incision may have occurred, but the data are inconclusive.

5.3. Timing of Terrace Formation

The minimum age of strath cutting is constrained by dating the depositional age and the abandonment age of terrace cover deposits on the Kashi, Atushi, and Mutule folds using 13 optically stimulated luminescence (OSL) ages and 1 cosmogenic depth profile, respectively. Measured ^{10}Be concentrations in the depth profile on the central Atushi fold decrease exponentially with depth (Table 4 and Figure S4). This observation is consistent with the absence of significant postdepositional sediment mixing and with a rapid and fairly steady sediment-accumulation rate compared to the age of the terrace. The age calculation requires some assumptions about the surface erosion or inflation rate of the gravel cover since abandonment. Judging from the

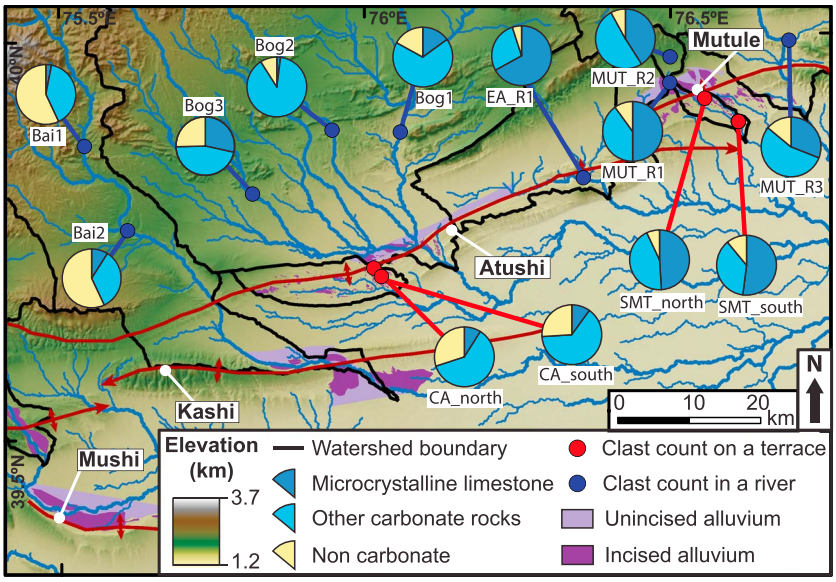

Figure 13. Lithologic clast counts in nine river locations and four terrace locations. For each location, 100–140 clast counts were sorted into three groups (see Text S2 and Table S2).

development of desert pavement (Figure S2c) and the preservation of primary fluvial topography on the terrace surface, we argue that erosion is negligible (≤10 cm). The presence of a ~30 cm thick horizon with an estimated 50% silt and gypsum (Figure S2b) suggests that surface inflation of ~15 cm by windblown dust (Kurth et al., 2011; Wells et al., 1995) is likely more important than deflation by erosion. Hence, in our cosmogenic analysis, we allow an inflation of 15 cm, an erosion of 10 cm, and erosion/inflation rates of ±1 cm/kyr. We further assign a range of gravel densities of 1.4–2.3 g/cm^3 (from typically reported values of loose and consolidated gravel) and a neutron attenuation length of 160 ± 5 g/cm^2 (Gosse & Phillips, 2001; Hidy et al., 2010). We calculate the most probable age after 2 × 10^5 iterations using a Monte Carlo simulator (Hidy et al., 2010) (Table S3). Ages using either a time-independent or time-dependent scaling scheme and either including or excluding the surface sample vary between 74 ± 17 ka (±2σ) and 89 ± 21 ka, respectively (Table S8). Any surface erosion or disintegration of larger pebbles into smaller pieces will cause underestimates of the surface age. Therefore, given uncertainties in the surface age, we use a mean abandonment age of 82 ± 19 ka (±2σ) and suggest excluding the surface sample entirely for the inheritance estimate.

Equivalent dose distributions for single aliquots of our OSL samples generally display high overdispersion (36–67%), and are significantly skewed (Table 5). These characteristics are commonly interpreted as signs of partial bleaching of the grains (Arnold et al., 2007; Bailey & Arnold, 2006; Kenworthy et al., 2014; Olley et al., 1998, 1999, 2004; Rhodes, 2011; Rittenour, 2008) (Table 5). Ages deduced from OSL dating vary depending on the age model used (Table 5). Based on the skewness and the overdispersion values, the minimum age model (MAM) is the most appropriate for all but two samples (Arnold et al., 2007) (Table 5). With two exceptions (Figures 15 and S5) sample ages from all dated terraces are in stratigraphic order with respect to the base level of the modern river (Figure 15).

Our terrace ages (all reported at ±2σ) provide minimum bounds on the time of the planation of the three studied structures (Figure 16). The highest terrace (T4) on the Kashi fold was formed at 48 ± 10 ka (Figure 16b). One terrace on western central Atushi was dated to 35 ± 7 ka (WCA-1, Table 5 and Figure 6) but is not considered in the remainder of the analysis because it was deposited by drainage internal to the fold. The most extensive and highest preserved fluvial gravels on western central Atushi yield an age of 82 ± 19 ka (Figure 16c). The high surface of the eastern Atushi fold that lies >200 m above local base level (Figures 5i, 5k, and 7d) remains undated but is likely older than 120 ka (Figure 16a). Finally, terraces on southern Mutule are dated to, respectively, 11 ± 3 ka (±2σ), 21 ± 7 ka, and 28 ± 7 ka (Figure 16d and Table 5). More recent beveling events can be observed on northern Mutule (Figure 16a), in the divot carved into the

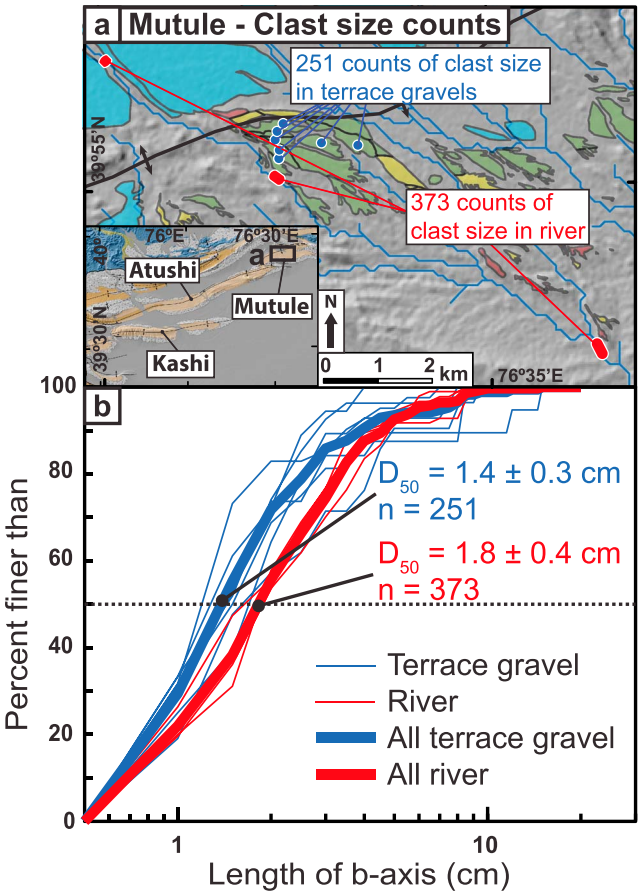

Figure 14. Counts of clast size with *b* axes >0.5 mm on Mutule fold. For each river location (red dots), ~125 clasts were counted at three nearby sites, yielding 373 counts per location. In the terrace gravels (blue dots), 20–60 clasts were counted at seven locations, totaling 251 clasts. (a) Map showing count sites on discrete terrace gravels on central Mutule. Color scheme for the terraces mimics Figures 9 and 12. (b) Particle-size distribution for individual terrace (blue) and river (red) counts (fine lines) with their mean (bold lines). D_{50} uncertainties estimated as 10% following Whittaker et al. (2011) and reported 2σ confidence intervals.

northern side of the Kashi fold (Figures 7 and 9), and across a ~20 km wide zone on the northern limb of western central Atushi (Figure 6). It is particularly striking that the Mutule fold, despite a recent episode of major beveling, is eroded by the smallest antecedent rivers (Figure 3) and that the beveled surface on the eastern Atushi fold (the youngest part of the eastward propagating Atushi fold (Chen et al., 2002)) has been abandoned for the longest time.

6. Discussion

This study's most significant finding is that kilometer-wide, low-relief surfaces preserved on the Kashi, Atushi, and Mutule folds provide evidence for intermittent beveling episodes characterized by very high ratios of lateral to vertical erosion rates. Such beveling episodes affect anticlines that are crossed by rivers with catchment areas ranging in size from <100 km^2 to 4,000 km^2, and we will demonstrate that they can be linked to order-of-magnitude increases in lateral erosion rates. Three key observations form the basis for the following discussion. First, a total of >2–6 km of rock uplift on the Kashi, Atushi, and Mutule folds (Figures 5a–5c), commonly <0.5 km of total aggradation on the surrounding alluvial fans (Figures 5a–5c), and a modern elevation of <800 m above the surrounding basin (Figures 5d–5o) imply efficient erosion of the uplifted rock throughout the 1 to 2 Myr long existence of the structures (Figure 5). Second, along structures with a uniform lithology, the contrast between wide, planar erosion surfaces and steep, convex hillslopes (Figures 5 and 6) suggests that variations in the erosion processes, instead of differences in lithology, climate, or tectonics, control the formation of the observed planation surfaces. This hypothesis is reinforced by clear topographic scarps and the boundaries between erosional surfaces that crosscut the strike of the structures (e.g., Figures 7b and 7c). Third, the presence of planation surfaces at a range of elevations (Figure 5) and formed at different times (Figures 15 and 16), and the occurrence of narrow canyons incised into these surfaces (Figures 6, 7, and 15) suggests that the folds are affected by temporal and spatial changes in the efficiency of lateral and vertical erosion.

Here we first discuss mechanisms of fold planation. Second, we derive rates of tectonic uplift, as well as lateral and vertical erosion, over the past 80 kyr, and we discuss the importance of aggradation in between the studied folds. Last, we explore potential drivers for the changes between fold planation and incision in the Tian Shan foreland on timescales of ~10–100 kyr.

6.1. Mechanisms of Fold Planation

6.1.1. Lateral Erosion by a Single Stream

Typically, planation surfaces are envisioned to form by the lateral migration of a single river. Such lateral erosion has been shown to occur by a combination of sweep erosion upstream of a channel narrowing (Bufe et al., 2016; Cook et al., 2014) as well as lateral erosion of valley walls along the length of an antecedent river (Bufe et al., 2016) (Figure 17). The "dent" in the northern Kashi fold and the simple terrace sequence on southern Kashi (Figures 7b, 9a, and 9c) are consistent with the erosion of the Kashi fold by a laterally migrating braided stream, not unlike the modern Baishikeremuhe that bisects the fold today.

6.1.2. Lateral Erosion by Multiple Streams

In contrast to the Kashi fold, the large extent of the surfaces on Atushi and Mutule, as well as the complex pattern of fluvial deposits preserved on them, suggests that these structures were beveled by multiple streams. We demonstrate that transitions between beveling and incision episodes are not commonly accompanied by major drainage reorganization events. The imbrication, moderate grain size, significant rounding,

Table 3
Clast-Size Counts on Mutule

Sample name	Latitude (°N)	Longitude (°E)	Elevation (msl)	Number of non-silt counts	$D_{50} \pm 1\sigma$ (cm)[a]	$D_{84} \pm 1\sigma$ (cm)[a]	Depth below terrace (m)	Approximate strike of face (deg)
SMT_R_south (start)	39.8879	76.6073	1,387	124	1.7 ± 0.2	3.5 ± 0.3	0	-
SMT_R_south (end)	39.8904	76.6058	1,332					
SMT_R_north (start)	39.9384	76.5010	1,747	124	1.9 ± 0.2	3.3 ± 0.3	0	-
SMT_R_north (end)	39.9378	76.5016	1,740					
SMT_R_central (start)	39.9189	76.5369	1,599	125	1.9 ± 0.2	4.1 ± 0.4	0	-
SMT_R_central (end)	39.9179	76.5387	1,596					
SMT_Terrace_1	39.9215	76.5383	1,618	27	1.5 ± 0.2	3.7 ± 0.4	0–4.8	Not measured
SMT_Terrace_2	39.9230	76.5384	1,635	26	1.3 ± 0.1	2.4 ± 0.2	1.1–2.3	Not measured
SMT_Terrace_3	39.9247	76.5376	1,629	60	1.2 ± 0.1	2.7 ± 0.3	3.1–4.3	60
SMT_Terrace_4	39.9260	76.5380	1,627	36	1.7 ± 0.2	2.8 ± 0.3	Not measured	20
SMT_Terrace_5	39.9273	76.5394	1,622	32	1.6 ± 0.2	4.4 ± 0.4	2.6–3.8	5
SMT_Terrace_6	39.9240	76.5475	1588	28	1.4 ± 0.1	3.0 ± 0.3	5.1–6.3	75
SMT_Terrace_7	39.9235	76.5553	1570	42	1.5 ± 0.1	2.4 ± 0.2	2.3–4.8	310–10
Mean of terrace counts	-	-	-	251	1.4 ± 0.1	2.9 ± 0.3	-	-
Mean of river counts	-	-	-	373	1.8 ± 0.2	3.6 ± 0.4	-	-

Note. msl, mean sea level.
[a]Calculated ignoring counts <0.5 cm; uncertainties are estimated as 10% following Whittaker et al. (2011).

and presence of planar beds and channels observed in the fluvial terrace cover (Figures 8, S2, and S3) are comparable to modern alluvial fan and river deposits and are consistent with a braided channel facies (Labourdette & Jones, 2007; Miall, 1977). Moreover, despite some modification, the surfaces of fluvial deposits show primary structures similar to channels traversing the modern alluvial fans. Finally, based on lithologic clast counts, the source areas of the gravels covering planation surfaces are similar to source areas of modern antecedent drainages (Figure 13) and the average imbrication directions of the fluvial deposits approximate the flow directions of modern streams (Figure 12). During active beveling, a veneer of gravel likely covered the entire fold surface as suggested by scattered remnants of gravels that can be found on the planation surfaces, as well as the barely incised, most recently beveled surfaces on northern Mutule and northern central Atushi (Figures 6, 7c, and 7e). In summary, these folds were most likely eroded by a multithreaded system of rapidly migrating braided rivers that are similar to the channels that cross the alluvial fans upstream of the structures today.

Table 4
Cosmogenic Nuclide Dating of Depth Profile CA-DP1

CA-DP: latitude: 39.7120°N; longitude: 76.0115°E; elevation: 1.5 km; height above modern river: 80 ± 20 (±2σ) m[a]; ^{10}Be standard: 07KNSTD[b]; ^{10}Be half live: 1.387 Myr

Sample name	Depth below surface ±2σ (cm)[c]	Quartz weight ± 1σ (g)[d]	^{10}Be carrier ±1σ (mg)[d]	^{10}Be/^{9}Be ± 1σ (10^{-14})[e]	^{10}Be concentration ± 1σ (10^{5} atoms/g)[f]
CA-DP1-surf	0	118.278 ± 0.005	0.185 ± 0.001	1086 ± 23	11.37 ± 0.25
Ca-DP1-0.3	30 ± 5	89.640 ± 0.005	0.197 ± 0.001	705 ± 12	10.37 ± 0.19
CA-DP1-0.6	60 ± 5	105.952 ± 0.005	0.197 ± 0.001	684 ± 20	8.49 ± 0.25
CA-DP1-0.9	90 ± 5	101.971 ± 0.005	0.200 ± 0.001	524 ± 16	6.86 ± 0.21
CA-DP1-1.2	120 ± 5	144.888 ± 0.005	0.197 ± 0.001	583 ± 11	5.30 ± 0.10
CA-DP1-1.6	160 ± 5	133.801 ± 0.005	0.196 ± 0.001	452 ± 11	4.42 ± 0.11
CA-DP1-2.0	200 ± 5	140.252 ± 0.005	0.196 ± 0.001	379 ± 7	3.54 ± 0.07
CA-DP1-3.0	300 ± 5	49.778 ± 0.005	0.198 ± 0.001	135 ± 4	3.61 ± 0.10

Note. See supporting information Figure S4 for graphical profile and age analysis.
[a]Absolute terrace and river elevations are estimated from a 90 m SRTM. Because the modern river is 5–9 km east of the terrace, the terrace elevations were detrended with the regional 0.7° slope (Figure 10). Uncertainty in the relative elevation is estimated from the precision of the DEM (Jarvis et al., 2008) and by recalculating the elevation difference for the range of line lengths. [b]Samples were measured at PRIME using a standard prepared by Nishiizumi et al. (2007). [c]CA-DP1-surf is from amalgamated pebbles spread out on the surface of the terrace. All other samples are from sand taken from 10 cm intervals within the depth profile. [d]Uncertainties are estimated from repeat measurements on the laboratory scale. [e]A mean blank ^{10}Be/^{9}Be ratio of $13.82 \pm 1.30 \times 10^{-15}$ measured from two laboratory blanks (^{10}Be/^{9}Be of $11.10 \pm 1.62 \times 10^{-15}$ and $16.53 \pm 2.00 \times 10^{-15}$) was subtracted from the measured ^{10}Be/^{9}Be ratio. Uncertainties are from uncertainties in the AMS measurement of samples and blanks. [f]Uncertainties include uncertainties in the ^{10}Be/^{9}Be ratio, the carrier mass, and the quartz weight.

Table 5
Results From Optically Stimulated Luminescence Dating of Fluvial Gravels

Sample name[a]	Latitude (°N)	Longitude (°E)	Fold	Terrace surface	Depth of sample below surface ±2σ (m)[b]	Elevation of terrace above modern river ±2σ (m)	Number of aliquots (accepted/total)	Dose rate ± 2σ (Gy/kyr)[c]	MAM age ± 2σ (ka)[d]	CAM age ± 2σ (ka)[d]	Overdispersion (%)	Skew	Kurtosis
CK-1	39.5643	75.9505	C Kashi	T4	1.4 ± 0.2	60 ± 10[e]	25/33	1.8 ± 0.1	15 ± 2	55 ± 14	61	0.5	−0.6
CK-2	39.5776	75.9480	C Kashi	T4	3.3 ± 0.2	95 ± 10[e]	22/29	1.7 ± 0.1	30 ± 4	**54 ± 8**	32	0.3	−0.7
CK-3	39.5785	75.9480	C Kashi	T4	3.9 ± 0.2	95 ± 10[e]	20/27	2.7 ± 0.1	23 ± 3	**41 ± 7**	36	0.4	−1.2
SMT-1	39.9195	76.5384	S Mutule	T2	1.3 ± 0.2	21 ± 1[f]	23/42	1.8 ± 0.1	**11 ± 3**	37 ± 11	67	1.1	0.6
SMT-2	39.9200	76.5393	S Mutule	T2	1.4 ± 0.2	23 ± 1[f]	21/35	2.2 ± 0.1	**11 ± 4**	38 ± 11	64	0.8	1.1
SMT-4	39.9114	76.5191	S Mutule	T3	6.0 ± 0.2	34 ± 2[f]	33/64	2.3 ± 0.1	**19 ± 5**	40 ± 8	52	1.1	0.7
SMT-5	39.9096	76.5183	S Mutule	T3	3.0 ± 0.2	34 ± 2[f]	23/38	2.6 ± 0.1	**23 ± 5**	47 ± 10	45	0.5	−0.4
SMT-6	39.9046	76.5833	S Mutule	T4	5.7 ± 0.2	59 ± 1[f]	33/47	2.7 ± 0.2	**31 ± 5**	54 ± 8	36	1.1	0.9
SMT-7	39.9043	76.5838	S Mutule	T4	7.0 ± 0.2	58 ± 1[f]	31/55	3.0 ± 0.2	**14 ± 3**	43 ± 9	56	1.4	1.8
SMT-8	39.9008	76.5918	S Mutule	T4	1.4 ± 0.2	57 ± 1[f]	20/27	3.0 ± 0.2	**13 ± 3**	26 ± 6	48	1.0	0.1
SMT-9	39.8907	76.6082	S Mutule	T4	5.3 ± 0.2	51 ± 1[f]	34/58	2.4 ± 0.1	**26 ± 5**	50 ± 8	42	1.0	0.3
WCA-1	39.6907	75.8513	WC Atushi	NA	1.0 ± 0.2	_[g]	21/49	2.3 ± 0.1	**35 ± 7**	61 ± 12	40	1.4	1.9
WCA-3	39.6907	75.8513	WC Atushi	NA	2.3 ± 0.2	_[g]	30/38	3.0 ± 0.2	18 ± 3	45 ± 9	49	1.4	2.5

Note. NA, not applicable.
[a]CK = central Kashi, SMT = south Mutule, EA = east Atushi, and WCA = west central Atushi. Samples marked in dark gray are characterized by a large U-series disequilibrium and are discarded.
[b]Uncertainties are estimated as ±20 cm on the basis of the scale of centimeter-scale undulations on the gravel cover surfaces and on the basis of repeat measurements of sample depths with the laser rangefinder. [c]The dose rate is calculated from radionuclide activities in representative samples measured through gamma ray spectroscopy and an estimated water content of 5 ± 5% (±2σ). Uncertainties are propagated from the standard deviations of radionuclide activities and the estimated uncertainties of the water contents. [d]Ages are obtained by applying the minimum age model and the central age model (Galbraith, 2005; Galbraith & Roberts, 2012; Galbraith et al., 1999) to the single aliquot equivalent dose data. Resulting equivalent doses are divided by the dose rate to obtain an age. Uncertainties are propagated from the dose rate uncertainty and equivalent dose standard error. Preferred ages are marked in bold print. [e]Absolute terrace elevations are taken from a differential GPS survey, whereas river elevations are estimated from a 90 m SRTM. Uncertainties in the elevation differences are estimated from the precision of the DEM (Jarvis et al., 2008) and by choosing multiple measurement locations on the terraces and modern streams. [f]Absolute terrace and river elevations are measured with differential GPS surveys. Their relative elevation is measured after projection of the data onto lines perpendicular to the fold axis (Figure 9). The variability of measurements along the projected lines (Figure 9) is used to estimate uncertainties. [g]Terraces appear to have been formed by rivers that drain the fold internally. The current elevation above that river is 15–25 m. However, the river profiles of fold internal rivers are likely changing more significantly with the uplift of the fold than rivers crossing the structure—we therefore ignore these data points.

6.1.3. Efficient Hillslope Erosion

As an alternative to fluvial erosion, efficient hillslope erosion through weathering, surface runoff, and aeolian processes (Rohrmann et al., 2013) could cause the described planation of topography. Indeed, many bedrock hillslopes on the Atushi Formation are covered by a centimeter-thick veneer of silt that was chemically weathered and/or physically eroded and redeposited on the slopes during rainstorms. Moreover, remnant beveled surfaces (now tilted to the north) on east central Atushi show large depressions and ridges aligned in what is likely the direction of the prevailing wind. Nonetheless, (1) well-preserved terrace cover or scattered remnants of fluvial gravels are preserved on parts of many beveled surfaces, and (2) the lithology, tectonic forcing, and local climate (rainfall and wind) are similar on the Kashi, Atushi, and Mutule folds, whereas the preservation of beveled surfaces is highly variable and sharp boundaries between subhorizontal erosion surfaces and steep, gullied hillslopes are found (e.g., Figure 7). Therefore, we deduce that fluvial erosion is clearly the dominant process in fold planation. Nevertheless, hillslope erosion modifies the planation surfaces once they are abandoned and incised, especially where fluvial gravels do not shield the underlying Atushi Formation from erosion.

6.1.4. Intermittent Episodes of Incision and Planation

Most modern planation surfaces are abandoned and incised by relatively narrow streams. Three lines of evidence suggest that repeated alternations between episodes of efficient lateral planation and episodes of rapid incision of the folds have affected the studied structures. First, the height of planation surfaces above the modern base level and the depth of incision into them varies greatly along the folds (Table 1). Second, the beveled surfaces are clearly of different ages (Figure 16) which is demonstrated by progressive tilting of terraces at different heights (Figures 9a and 9c) (Heermance et al., 2008; Scharer et al., 2006) and our terrace dating (Figures 15 and 16). The third line of evidence for intermittent episodes of beveling and incision is the meter-scale topography of the planation surface preserved beneath the fluvial deposits (Figures 8 and 11). For example, a stringer of 10 to 20 m thick gravel (T4) that extends nearly 6 km downslope across the Mutule fold and is buttressed against the bedrock (Figure 8b and Figure 12a: T4) is interpreted as a paleocanyon and consistent with an episode of >10 m of incision predating the T4-planation episode. We, therefore, conclude that episodes of beveling and incision have likely alternated on these folds for an extended period of time—possibly across the entire time of their emergence above the depositional surface.

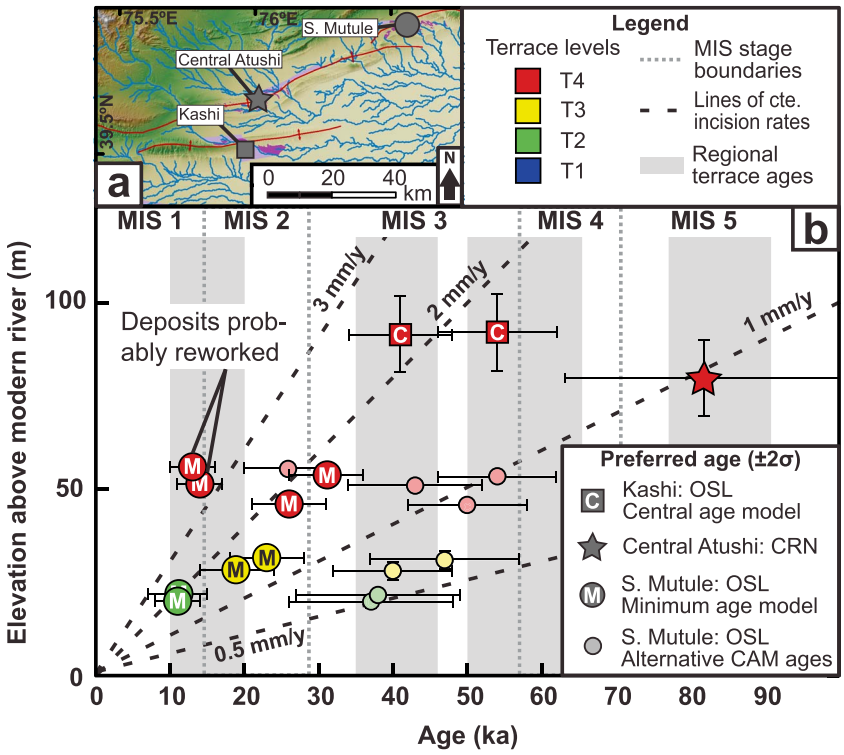

Figure 15. Terrace ages (with 2σ uncertainties) as a function of height above modern rivers. (a) Overview map showing locations of dated surfaces. See Figure 6 for sample locations. (b) Terrace ages versus height above the modern river. Preferred sample ages are marked with darker colored symbols (cf. Table 5). For samples where the minimum age model (M) was preferred, the central age model (C) result is plotted as a lighter-colored, smaller data point. Sample height above the modern river combines the terrace height above the modern river with the sample depth below the terrace surface. Dashed black lines mark expected elevations as a function of age for a range of uplift/incision rates. The dotted gray lines are the boundaries of the marine isotope stages based on Lisiecki and Raymo (2005). The light gray bars mark clusters of published ages of fan, basin, and terrace gravels in the region (Li et al., 2012, 2013; Thompson Jobe et al., 2017).

6.2. Rates of Vertical and Lateral Erosion

Transitions between episodes of fold incision and episodes of fluvial planation have to be driven by a change in the ratio of vertical erosion rates (E_v) to horizontal (lateral) erosion rates (E_h) (Figure 1). These rates are set by a potentially complex interaction of rock-uplift rates, sediment and water fluxes, and autogenic dynamics. In order to simplify the problem, we make two important evidence-based assumptions: first, we assume that the along-stream profiles of the channels crossing the folds did not change appreciably over the relevant timescales of 10–100 kyr. By appreciable changes, we refer to long-lived (tens of kiloyears) and high-amplitude (tens of meters) changes in the relative heights across the stream profile that would challenge any interpretation of the observed terrace incision as revealing some long-term uplift signal. It is difficult to prove this assumption, but substantiating evidence can be found in the similarity between the slopes of the top of the terrace cover on Mutule and the associated modern river (Figures 9b and 9d). If this assumption holds, we can further assume that, on the timescales relevant for fold planation or fold incision (2 to <30 kyr, see below), vertical erosion rates (E_v) match the rock-uplift rate (U) of the structure above the surrounding alluvial fans:

$$E_v = U - G \tag{7}$$

(Figure 17). Here G is the surface-uplift rate of the surrounding basin due to sediment aggradation. If incision rates into a growing structure were faster than the rock-uplift rates of the structure above the surrounding aggrading basins, ($E_v > U - G$), the fans upstream and downstream of the structures would be incised. Even though most planation surfaces have been recently incised, no evidence exists for such incision upstream or downstream of the folds (Figures 6, 7, and 9). Of course, we cannot exclude fan incision and subsequent refilling during older incision and beveling cycles (>30–80 ka). If incision rates were slower

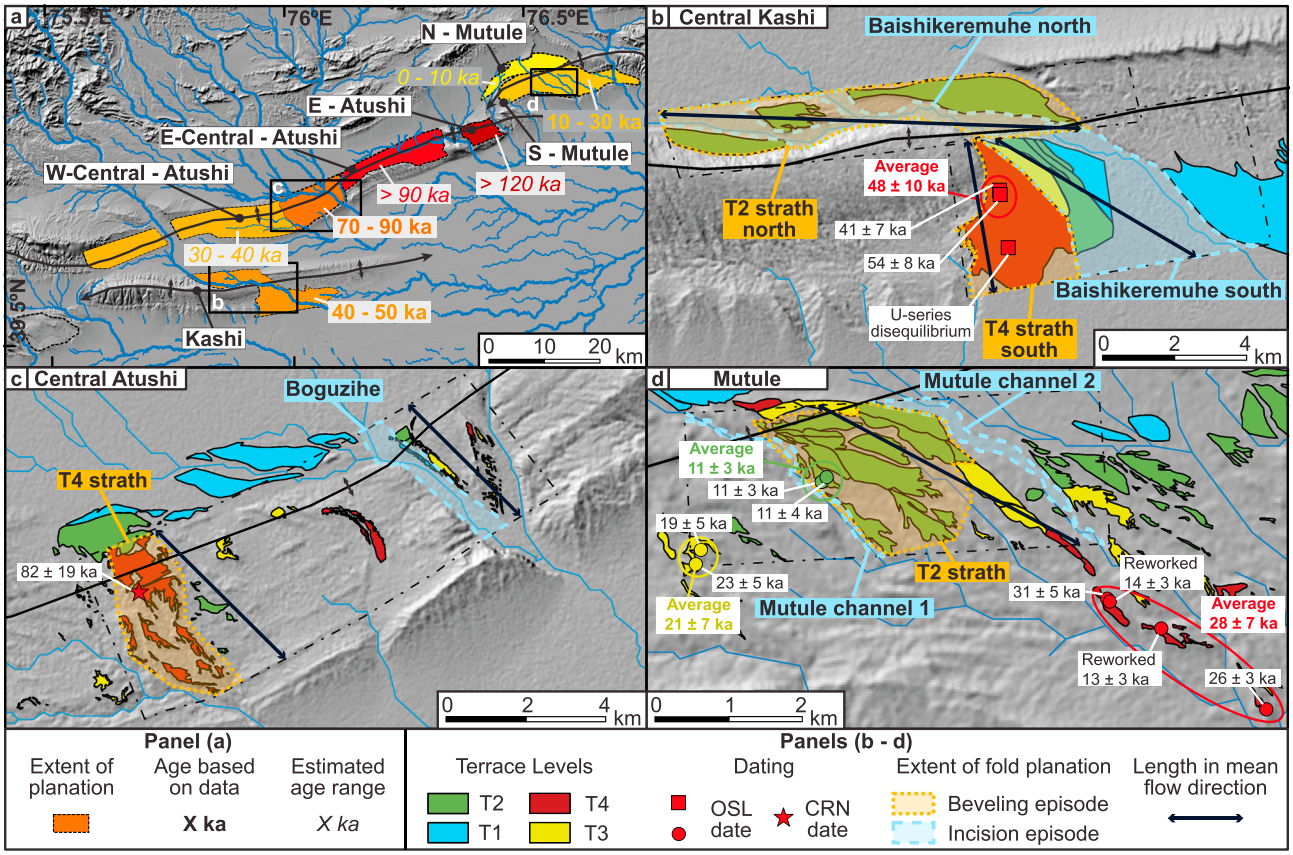

Figure 16. Summary of ages (2σ uncertainties) of beveled surfaces and areas used for the calculation of beveling rates. (a) Overview of the main beveled areas in the region with darker colors showing older surfaces. The age ranges correspond to the oldest major beveling episode preserved. Most surfaces (such as the surfaces on the Kashi fold) have been partly reworked by younger planation episodes. Black squares show the locations of Figures 16b–16d. (b–d) Mapped strath terrace cover on Kashi, Atushi, and Mutule fold showing the dates from OSL and CRN dating. Also shown are area estimates for well-preserved strath terraces and areas of modern river valleys used for calculating beveling rates (light orange and light blue transparent areas; see Table 7 for calculations). Fine, black, and dash-dotted lines mark the fold area over which these calculations were made. The mean flow direction in which the length of the beveled surface is measured (black arrows) is estimated on Atushi and Mutule from imbrication measurements and on Kashi from the orientation of terraces.

than the rock-uplift rates above the aggrading basins, ($E_v < U - G$), rivers would eventually be defeated and flow around the structures or form lakes behind them. The Baishikeremuhe crossing the Kashi fold is the only stream for which evidence of periodic defeat exists such that the above assumption might not hold. However, since at least the time of deposition of the T4 terrace on Kashi (48 ± 10 ka), equation (7) should

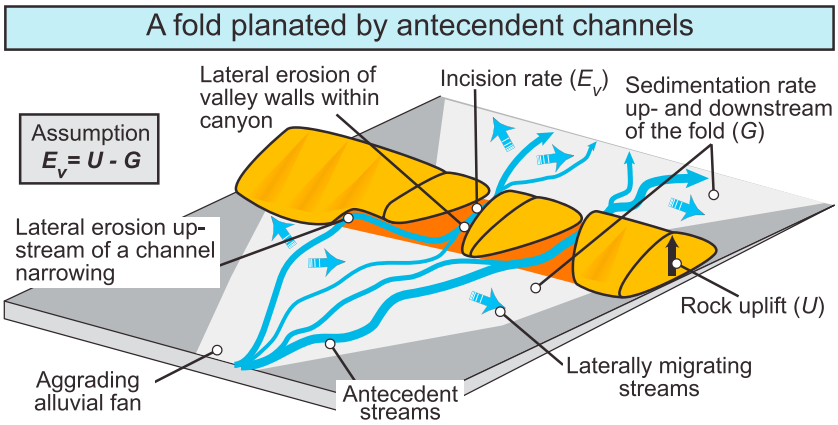

Figure 17. Conceptual sketch of the beveling mechanisms of a fold.

be valid for all structures in the study area. Note that in equation (7), aggradation rate has to be corrected for the differential subsidence of the alluvial fans either side of the fold with respect to the uplifting structure. However, subsidence on the scale of the entire foreland basin, which affects the folds and the adjacent alluvial fans equally, does not affect the calculation.

Assuming that equation (7) holds, we can substitute it into equations (3) and (4) and rephrase the average areal planation rates (equations (1), (2), (5), and (6)) in terms of uplift and aggradation rates. For incision episodes

$$P_i = \frac{(U - G)\, A_i}{D_i} \tag{8}$$

$$E_{\mathrm{hi}} = \frac{(U - G)\, A_i}{L\, D_i} \tag{9}$$

and for beveling episodes:

$$P_b \geq \frac{(U - G)\, A_b}{H_b} \tag{10}$$

$$E_{\mathrm{hb}} \geq \frac{(U - G)\, A_b}{L\, H_b}. \tag{11}$$

Thus, over kiloyear timescales, we can discuss the impact of changes in rock-uplift rates and aggradation rates on the ratio of lateral and vertical erosion rates.

6.2.1. Average Rates of Rock Uplift in the Foreland of the Tian Shan

Equations (7)–(11) show that in order to constrain rates of lateral planation on kiloyear timescales, rock-uplift rates of the folds and aggradation rates in the foreland over the same kiloyear timescales have to be constrained. Since initiation of fold growth, as determined by the first appearance of growth strata 1–2.5 Myr ago, average rock-uplift rates of the Kashi, Atushi, and Mutule folds have been constrained to 1–4 mm/yr (Bufe et al., 2017; Chen et al., 2007; Heermance et al., 2008). However, rock-uplift rates over the past 30–80 kyr (the timing of the most recent fold planation episodes) remain poorly constrained. Here we complement terrace surveys from previous studies showing that abandoned terraces on the Mushi, Mingyaole, Kashi, and Atushi folds are commonly tilted or otherwise deformed by increasing amounts with age due to the ongoing growth and uplift by the folds (Figure 9) (Figures 8, 9, 11 in Scharer et al., 2006, Figure 13 in Heermance et al., 2008, and Figure 8 in Li et al., 2013). In the absence of (1) significant incision of the modern alluvial fans in the foreland of the Tian Shan or (2) evidence for river diversions across structures or major lake formation, we assume that equation (7) holds (incision rates equal rock-uplift rates minus surface-uplift rates) and interpret the incised and tilted terraces as recording average rock-uplift rates of the folds (relative to the slowly rising base level resulting from foreland aggradation) throughout the Late Quaternary. On the western Mutule fold, tilting with respect to the modern river is not clear (Figures 9b and 9d), likely because total uplift since terrace abandonment (deduced from the depth of incision) is small compared to the other folds (Table 1) and because fluvial deposits on straths are not preserved across much of the fold limb and largely occur within the bounds of a single dip domain (Figure 9). Moreover, if the fold deforms primarily by hinge migration (Li et al., 2015a), rather than limb rotation, differential rotation is not expected except for the outer hinge (Scharer et al., 2006). Evidence for continued uplift on Mutule is, nonetheless, strong, because (1) alluvial fans upstream of Mutule are not incised, (2) strath terraces sit as much as 50 m above modern base level across the fold, and (3) aggradation by $>$50 m (the height of T4 on Mutule) of the entire area north of Mutule and subsequent stripping by a similar amount without leaving erosional remnants is unlikely. Thus, the Late Quaternary ages of the terraces dated in this study and the differential tilting of terraces on the Kashi (Figure 9c) and Atushi folds (Scharer et al., 2006) imply that the folds in the foreland of the Tian Shan have been actively uplifting during the Quaternary.

Terrace ages on Kashi, Atushi, and Mutule define a trend of increasing ages with height above the modern river (Figure 15). Average rock-uplift rates were estimated by dividing the difference in height between the highest and lowest terrace top by their age difference (Table 6). Where only one terrace level was dated (Atushi and Kashi), we used the age and the height above the modern river to estimate uplift rates (Table 6). Note that, in case of the Kashi fold, we projected the tilted T4 terrace (Figure 9) to the core of the anticline to estimate a peak incision/uplift rate (Table 6). We disregard samples WCA-1, and WCA-3 in

Table 6
Average Incision/Uplift Rates of Kashi, Atushi, and Mutule

Structure[a]	Interval considered[b]	Depth of incision ±2σ (m)[c]	Duration of incision ±2σ (kyr)[d]	Average incision rate ± 2σ (mm/yr)
Kashi	T4 terrace peak-modern river	130 ± 20	48 ± 10	**2.7 ± 0.7**
Kashi	T4 sample-modern river	95 ± 10	48 ± 10	2.0 ± 0.5
Atushi	T4 peak/sample-modern river	80 ± 20	82 ± 19	**1.0 ± 0.3**
Mutule	T4 peak/sample-modern river	55 ± 1	28 ± 4	2.0 ± 0.2
Mutule	T3 peak/sample-modern river	34 ± 1	21 ± 4	1.6 ± 0.3
Mutule	T2 peak/sample-modern river	22 ± 1	11 ± 3	2.0 ± 0.5
Mutule	T4 peak/sample-T3 peak/sample	21 ± 2	7 ± 5	3.0 ± 2.2
Mutule	T4 peak/sample-T2 peak/sample	33 ± 1	17 ± 4	**1.9 ± 0.5**
Mutule	T3 peak/sample-T2 peak/sample	12 ± 2	10 ± 4	1.2 ± 0.5

[a]For each structure (except Atushi) multiple estimates of average incision rates are given. The incision rate that best estimates average uplift rates of the structure is marked in bold print. [b]Intervals considered in the analysis are either an interval between a terrace gravel top and the bed of the modern river or between two terrace gravel tops. [c]Terrace elevations above the modern river are taken from averages of the terrace elevation estimated at the sample sites (cf. Table 5 for Kashi and Mutule and Table 4 for Atushi). The T4 elevation on the crest of the Kashi fold (T4 peak) is estimated by extrapolating the terrace and river slopes (shown in Figure 9) up to the fold crest. An additional iuncertainty of ± 10 m is estimated due to this extrapolation. [d]Duration of incision is estimated by assuming ages represent terrace abandonment ages.

this analysis, because the strath terrace on western Atushi was not clearly cut by a river crossing the fold but was probably created by fold-internal drainage, thereby complicating the interpretation of the base level. Using the preferred OSL age models, we estimate average surface-uplift rates above the aggrading base level of 2.7 ± 0.7 mm/yr (±2σ) for Kashi, ~1.0 ± 0.3 mm/yr for Atushi, and ~1.9 ± 0.5 mm/yr for Mutule since between ~80 and ~30 ka (Figure 15 and Table 6). We note that this range of incision/uplift rates is decreased by ~0.5 mm/yr for Mutule if the central age model is used for all samples (Figure 15). These rates are similar to the million-year rock-uplift rates for the Kashi fold (Bufe et al., 2017; Chen et al., 2007;Heermance et al., 2008 ; Scharer et al., 2004). In contrast, rock-uplift rates on the Atushi and Mutule folds likely decreased from rates of >3–4 mm/yr close to their initiation ~1–1.4 Myr ago, to average rates of 1–2 mm/yr over the past 30–80 kyr (Bufe et al., 2017). The calculated incision/uplift rates are averages across timescales of 30–80 kyr, and uplift rates could vary on shorter timescales. The Kashi, Atushi, and western Mutule folds have previously been interpreted as aseismically (and, therefore, likely steadily) deforming detachment folds (Heermance et al., 2008; Scharer et al., 2004). However, a small surface-rupturing fault has been recognized just north of the water gap on central Atushi (Figure 4) and new seismic data (Gao et al., 2013; L. Tao, personal communications, 2017) may lead to a reinterpretation of the fault control on the structures. Therefore, changes in uplift rates, for example, due to earthquake cycles, cannot be ruled out. Moreover, episodes of relative tectonic quiescence with durations of several tens of kiloyears have been interpreted on some slowly growing, thrust-controlled anticlines (Gunderson et al., 2014). However, given the high average uplift rates of ≥1 mm/yr calculated across the past 30–80 kyr (Table 6), the scarcity of modern seismicity on these structures (Bufe et al., 2017; Li et al., 2012), and the occurrence of multiple series of differentially uplifted terrace sequences, an intermittency of uplift rates on timescales much longer than a few kiloyears, appears unlikely. We, therefore, conclude that the terraces in the foreland of the Tian Shan record continuous uplift of the Atushi, Kashi, and Mutule folds on timescales of tens of kiloyears and at rates that are broadly comparable to million-year averages.

6.2.2. Sediment Aggradation Between Folds

Average sedimentation rates in the Kashi Basin between 3.4 Ma and 0.8 Ma have been calculated to be on the order of ~0.3–0.8 mm/yr (Chen et al., 2007; Heermance et al., 2007), but basin-wide aggradation rates and their variation over latest Quaternary timescales are currently unconstrained. As mentioned above, Late Quaternary incision/rock-uplift rates of 2.7 ± 0.7 mm/yr for Kashi, ~1.0 ± 0.3 mm/yr for Atushi, and ~1.9 ± 0.5 mm/yr for Mutule are measured with respect to the aggrading basin floor. We argue that it is unlikely that average aggradation rates across 30–80 kyr exceeded 1 mm/yr. However, the few remnant patches of >0.5 m thick fluvial gravels preserved on selected areas of the folds may indicate that locally, short pulses of rapid aggradation could outpace uplift rates. The most striking example is a 20 m thick and ~100 m wide deposit along the length of southern Mutule (Figure 12a), which we interpret as an infilled paleocanyon.

With the exception of above mentioned paleocanyon, the buried topography beneath all measured fills is much less than the height differences (10–280 m) between canyons and hilltops observed during the current fold incision. Therefore, we assume that the fills formed either during or shortly after a beveling episode. In the case that thick fills form toward the beginning of a beveling episode, the buried bedrock topography of ~6 ± 2 m (Figures 2 and 12) could represent the remnants of an incised older planation surface that was modified by incision and hillslope retreat before being partly infilled and partly planed off. In this case, the measured height variations would be an overestimate of the topography of a typical planation surface. Alternatively, the buried topography could represent the height differences along the active channel bed during planation, and the fills could be the bedload of those planating rivers (Figure 2). This scenario seems unlikely where gravel thickness exceeds more than 5–10 m, as in the described paleocanyon (Figure 12), but probably applies to the large areas that currently preserve thin, discontinuous, or scattered gravel remnants. Finally, major aggradation events could occur toward the end of the planation episode and just before abandonment and incision of the terraces. Here the measured topography would also be representative of the height variations on the planation surface. Whereas we cannot distinguish among the different scenarios, in all cases the age of the gravels is close to coeval with the planation episode and the height differences of the buried topography (typically ~6 ± 2 m) represent maximum estimates of the topography on the planation surfaces (H_b in equations (4), (10), and (11) and Figure 2). We assume that the likelihood of preservation of the gravel is a function of its thickness. If this is true, the extensive planation surfaces on Atushi and Mutule that are bare of fluvial deposits (Figure 6 and Table 1) indicate that rapid aggradation events were spatially limited and did not control beveling across the entire study area. Moreover, these pulses were clearly limited in time (otherwise there would be no net bedrock uplift above the basin floor), and average aggradation rates on kiloyear timescales have to be much smaller than uplift rates.

We conclude that average aggradation rates across the foreland have likely been much smaller than average uplift rates on timescales of tens of kiloyears and that short ($\ll$10 kyr) pulses of rapid aggradation that outpace uplift rates were locally restricted and did not control the formation of planation surfaces across all structures in the foreland of the Tian Shan. Furthermore, in order to bevel such remnant surfaces that are tens of kilometers wide in directions perpendicular to the paleoflow, rivers needed "access" to the uplifting bedrock. The broad planarity of these beveled surfaces suggests shallow, commonly avulsing channels would be prevalent.

6.2.3. Rates of Lateral Erosion and Duration of Beveling Episodes

One major implication of the presence of extensive beveled platforms, on the one hand, and incised channels, on the other, is that large changes in the ratio of lateral to vertical bedrock erosion rates are necessary to explain the extensive beveled surfaces. Commonly, strath-terrace formation has been interpreted to be driven by changes in vertical incision rates (DeVecchio et al., 2012; Fuller et al., 2009; Gilbert, 1877; Hancock & Anderson, 2002; Langston et al., 2015; Merritts et al., 1994; Molnar et al., 1994; Pan et al., 2003; Zaprowski et al., 2001). Here we argue that in the Tian Shan foreland, variations in lateral bedrock erosion rates are necessary to explain the extent of the planation surfaces. Vertical incision rates may also vary, but their variation is not necessary to explain the beveled platforms.

In order to support this argument, we use equations (1)–(4) to estimate an average areal planation rate during incision (P_i) and beveling (P_b) episodes on four selected surfaces on Kashi, Atushi, and Mutule. Surfaces are selected where the beveled area and the modern streams that cut them can be reliably reconstructed (Figure 16). For channel incision episodes, an average incision rate deduced from the abandonment age of terraces (E_{vi}) adjacent to the canyon (Table 6), an incision depth (D_i) calculated using a DEM or field surveys (Table 6), and a canyon area (A_i) mapped on a DEM (Figure 16 and Table 7) are used. When measuring A_i, we assume that the area occupied by river channels and the area eroded by hillslope erosion is negligible. The former assumption is violated in narrow canyons in which all, or a significant proportion of the total canyon area, is not formed by the lateral migration of a stream but represents the width of the channel during floods. Therefore, lateral planation rates during incision episodes are probably overestimated. We find that streams could not have planated areas at average rates faster than 300 ± 90 to 350 ± 150 m^2/yr on Kashi, 50 ± 20 m^2/yr on Atushi, and a total of 70 ± 14 m^2/yr on Mutule (Table 7). These lateral erosion rates during channel incision are independent of the temporal evolution of uplift/incision rates of the structures and depend only on the time since incision started (in addition to the canyon depth and beveled area)—a time that is constrained by our terrace ages (Figure 16 and Table 6).

Table 7
Calculation of Planation Rates for Incision and Planation Episodes

Lateral bedrock erosion rates during planation episodes and during incision episodes								
Landform	Fold	Peak uplift rate (U) ±2σ (mm/yr)	Maximum incision depth (D_i or H_b) ±2σ (m)[a]	Duration of episode (Δt) ±2σ (kyr)[b]	Planated area (A) ±2σ (km2)[c]	Areal planation rate (P) ±2σ (m^2/yr)	Flow-parallel length (L) ±2σ (km)[d]	Lateral bedrock erosion rate (E_h) ±2σ (mm/yr)[e]
Incision episode (modern rivers)								
Baishikeremhue	North Kashi	2.7 ± 0.7	45 ± 15	17 ± 7	5.8 ± 0.3	350 ± 150	11.6 ± 0.6	30 ± 13
Baishikeremhue	Central/south Kashi	2.7 ± 0.7	130 ± 20	48 ± 14	14.5 ± 0.7	300 ± 90	6.3 ± 0.3	48 ± 15
Boguzihe	Atushi	1.0 ± 0.3	50 ± 10	51 ± 18	2.4 ± 0.1	47 ± 17	4.1 ± 0.2	12 ± 4
Mutule channel 1	Mutule	1.9 ± 0.5	22 ± 1	11 ± 3	0.2 ± 0.0	22 ± 6	4.3 ± 0.2	5 ± 1
Mutule channel 2	Mutule	1.9 ± 0.5	22 ± 1	11 ± 3	0.5 ± 0.0	46 ± 13	4.3 ± 0.2	11 ± 3
Beveling episodes								
T2 strath	North Kashi	2.7 ± 0.7	6 ± 2	2 ± 1	14.7 ± 7.3	6,600 ± 4300	11.6 ± 0.6	570 ± 370
T4 strath	Central/south Kashi	2.7 ± 0.7	10 ± 5	4 ± 2	8.3 ± 0.8	2,300 ± 1300	4.3 ± 0.2	520 ± 300
T4 strath	Atushi	1.0 ± 0.3	6 ± 2	6 ± 3	6.7 ± 2.0	1,100 ± 600	4.8 ± 0.2	230 ± 120
T2 strath	Mutule	1.9 ± 0.5	6 ± 2	3 ± 1	3.7 ± 1.1	1,200 ± 600	4.3 ± 0.2	280 ± 150

[a]Incision depth for modern rivers are measured from the top of gravel-covered straths to the modern riverbed and obtained from differential GPS surveys (Mutule, Baishikeremuhe south - see Table 6) or estimated from Google Earth® (Boguzihe, Baishikeremuhe north). Uncertainties for the Google Earth ®measurements are estimated from the precision of the DEM (Jarvis et al., 2008) and by choosing multiple measurement locations on the terraces and modern streams. The incision depth for planation surfaces is estimated from measured strath relief (Mutule and Atushi) or estimated (Kashi) (see text). [b]Calculated from peak uplift rates and maximum incision depths by assuming incision rates are equal to average uplift rates. For the sake of consistency, we propagated the errors from the peak uplift rate and the incision depth even for the Baishikeremuhe south and the Mutule channels for which the duration is known from the OSL data. [c]Uncertainties estimated by measuring areas of a series of reasonable polygons (see Figure 16). [d]The straight line length of channels and planation surfaces are measured in the (measured or estimated) average direction of flow (see Figure 16). Uncertainties are estimated by choosing a range of reasonable flow directions. [e]These lateral bedrock erosion rates are rates equivalent to one or several straight channels linearly eroding the sides of a canyon wall (see text for details).

In order to calculate areal planation rates during beveling episodes using equations (2) and (4), we only use surfaces that are covered with fluvial gravel to estimate the total beveled area (A_b) (Figure 16 and Table 7). Again, we assume that the area occupied by river channels and the area eroded by hillslope erosion is negligible. Maximum height differences across the strath (H_b) are taken as 6 ± 2 m for all folds as discussed above, but the average vertical incision rate during beveling episodes (E_{vb}) is unknown. Here let us assume that average uplift and aggradation rates did not change across the relevant time period (Table 7). Using this assumption, we obtain average areal planation rates of 2,300 ± 1,300 to 6,600 ± 4,300 m^2/yr on Kashi, 1,100 ± 600 m^2/yr on Atushi, and 1,200 ± 600 m^2/yr on Mutule folds during at least 2 to 6 kyr long beveling episodes (Δt_b) (Table 7). Such rates are more than 1 order of magnitude (20–50 times) higher than areal planation rates during the 10 to 50 kyr long incision episodes (Δt_i). We reiterate that Δt_b merely represents the time during which each point on the planation surface has to be revisited and that the duration of the beveling episodes could have been much longer than Δt_b if the rivers frequently changed the direction of lateral movement and moved back and forth across the surface. Moreover, planation rates during beveling episodes on the Atushi and southern Mutule folds are likely to have been up to several times higher than estimated here, because the measured extent of strath surfaces used in this calculation is limited to the area where fluvial gravels are preserved: an area representing $<$20% of the beveled area on these folds (Figure 16). Similar results are obtained when lateral erosion rates equivalent to a single straight laterally eroding stream are calculated using equations (5) and (6): An average flow direction can be deduced from imbrication measurements (on Atushi and Mutule) and from the orientation of the terraces (on Kashi), and a length of the planated area (L) parallel to that flow direction can be measured on a DEM (Figure 16 and Table 7). The resulting minimum lateral bedrock erosion rates of 0.2–0.6 m/yr (E_{hb}) (Table 7) are more than an order of magnitude higher than planation rates of 0.005–0.05 m/yr (E_{hi}) during times when vertical channel incision of the folds dominates (Table 7). Results from sandbox experiments support such planation rates exceeding 0.2 m/yr during beveling episodes (Bufe et al., 2016). When these experiments are scaled-up to the dimensions of the folds in the Tian Shan, they suggest that, in order to explain the wholesale beveling of the Atushi fold, lateral bedrock erosion rates of several meters per year are necessary (Bufe et al., 2016). Importantly, these experiments demonstrated that significant changes in lateral erosion rates can occur without any change in vertical incision rates due to variability in the lateral channel mobility of a river that is incising at a constant rate into an uplifting fold (Bufe et al., 2016).

The planation rates during beveling episodes calculated above rest on the assumption that average vertical incision rates are constant when calculated over timescales of >2–6 kyr (the duration of the beveling episodes). Any changes in vertical incision rates that act on timescales shorter than 2–6 kyr would not affect above calculation, as long as the average incision rates do not change across the interval. As an end-member scenario alternative to steady incision, vertical incision rates could cease entirely during beveling episodes. In order to explain the beveled platforms without any changes in lateral erosion rates, fold incision would have to cease for >42 ± 28 kyr, 28 ± 9 kyr, 141 ± 66 kyr, and 54 ± 22 kyr on, respectively, northern Kashi, southern Kashi, Atushi, and Mutule (Table 7). As long as equation (7) (incision rates = uplift rates − aggradation rates) holds true, such long episodes without any uplift or with very rapid aggradation seem untenable with our observations, and therefore, increases in the lateral erosion rates of streams are required to explain the extent of the observed beveled platforms. We cannot rule out a cessation of incision during beveling episodes. Indeed, because vertical incision and lateral erosion are in part affected by similar controls (such as the ratio of transport capacity and sediment flux), incision rates might be expected to be at least reduced during times of fold planation or characterized by episodes without incision and short pulses of rapid vertical erosion. However, unless incision ceased entirely for ≫2–6 kyr, order of magnitude changes in lateral erosion rates have to have occurred. In turn, to explain the existence of the beveled platforms without any change in lateral erosion rates, vertical incision rates would have to stop for 30–140 kyr. Importantly, any possible change in average incision rates of a few millimeters per year during planation episodes is small compared to changes of tens of centimeters per year in the average rates of lateral erosion. Therefore, in the foreland of the Tian Shan, changes in the average lateral erosion rates appear to be the dominant control on the size, rate, and timing of strath terrace cutting.

Caution is warranted when extending these results to different settings. Bedrock strength has a significant effect on the lateral erosion rates and the size of planation surfaces has been linked to bedrock lithology (Allen et al., 2013; Montgomery, 2004; Römer, 2010; Schanz & Montgomery, 2016). Whereas narrow strath terraces have been documented in more resistant lithologies, such as granites and quartzite (Burbank et al., 1996; Pratt-Sitaula et al., 2004), most wide planation surfaces form in weak or weathered lithologies (Allen et al., 2013; Brocard & van der Beek, 2006; Collins et al., 2016; Cook et al., 2014; Fuller et al., 2009; Hancock et al., 1999; Langston et al., 2015; Lavé & Avouac, 2001; Molnar et al., 1994; Montgomery, 2004; Schanz & Montgomery, 2016). As a perturbed fluvial system adjusts toward a new equilibrium, lateral erosion rates of bedrock topography can reach tens of meters per year (Anton et al., 2015; Bufe et al., 2016; Collins et al., 2016; Cook et al., 2014) even in resistant lithologies, such as unweathered granite (Anton et al., 2015) and, thus, can match river migration rates on alluvial plains (Jerolmack & Mohrig, 2007). Hence, whereas the absolute lateral erosion rates are typically lower and planation surfaces narrower where rock strength is high, accelerated lateral erosion rates can likely cause strath-terrace formation even in such settings.

6.3. Drivers for Changes in Lateral Planation Rates

Two questions are addressed here: (1) what controls the changes between lateral planation and canyon cutting within one catchment (temporal differences) and (2) what controls the differences in beveling history among different catchments (spatial differences)?

6.3.1. Changes From Lateral Planation to Incision

Commonly, climatically induced changes in sediment or water fluxes or the frequency of floods are evoked as drivers for changes in both lateral and vertical erosion rates. However, correlating the record of beveled surfaces directly with documented regional climatic changes that would explain variations in the water and sediment influxes or the flood frequency appears untenable with our data. Our terrace ages cannot be consistently correlated with trends in the marine isotope stage record (Figure 15) (Lisiecki & Raymo, 2005; Petit et al., 1999) or with clusters of terrace and alluvial fan ages from other deposits in the region (Li et al., 2012, 2013; Thompson Jobe et al., 2017; Yang & Scuderi, 2010) (Figure 15). The number of samples in this study is small with respect to the size of the beveled surfaces, and large areas on the folds remain undated. Perhaps, a more detailed and thorough dating of planation surfaces or more extensive hydrologic data would reveal an overall climate dependency. In any case, the temporal differences among the planation surfaces across folds in the study area exclude a simple scenario of regional climatic changes causing coeval rapid lateral planation on all folds. Moreover, the absence of evidence for major cut-and-fill sequences on the alluvial fans upstream and downstream of the folds support the interpretation that basin-wide sediment fluxes and aggradation rates were most likely relatively steady over timescales of tens of thousands of years. However, we note

that, if the central age model (CAM) were used for the Mutule samples, all terrace ages, except for the Atushi terrace, would fall within MIS3 (Figure 15) and might indicate a climatic control on strath formation.

Independently of the regional climate, linking planation episodes in each catchment directly to changes in the sediment and water fluxes is difficult, especially if such changes are small, short, or infrequent. Two possible measures are clast sizes of the fluvial sediment (as a recorder of water and sediment fluxes) or erosion rates in upstream catchments (as a proxy for higher sediment fluxes to the basin). Clast sizes in the modern rivers are coarser than on the terrace gravels by a factor of 1.3. However, as discussed above, D_{50} values are within 2σ uncertainties of each other (Figure 14). Moreover, comparing bed material at the surface of the modern river with material from the subsurface of the paleoriver (the terrace gravels) can be inappropriate, because a coarsening of the modern surface is expected if the transport capacity exceeds the sediment load (Dietrich et al., 1989; Montgomery et al., 1999). Thus, the difference in D_{50} values between river and terrace cover (Figure 14) could be explained without any change in the hydrology between the past and the present. Alternatively, the small grain-size difference could arise from changes between an aggrading and an incising river. Moreover, the size of the input sediment in modern rivers could have increased due to grain size-modulating processes in the upstream catchments, for example, tectonic perturbations or changes in vegetation (Whittaker et al., 2010). Finally, a coarsening of modern surface deposits by a factor of 1.3 could be explained by a reduction of sediment supply of 10–80% with respect to the water supply (Dietrich et al., 1989). More clast-size data are necessary to confirm the presence or absence of a trend. Measuring changes in catchment-wide mean erosion rates, as a proxy for sediment flux (Davis et al., 2012; Hidy et al., 2014; McPhillips et al., 2013; Schaller et al., 2002, 2004; Schaller & Ehlers, 2006; Wittmann et al., 2010), between times of fold planation and fold incision using cosmogenic nuclide dating is the subject of ongoing work by the authors and preliminary results appear to suggest that no significant differences in catchment-averaged erosion rates measured in modern stream sediment and in terrace deposits can be detected.

A proliferation of terraces across a range of regional climates is consistent with experimental findings that relatively small perturbations of the fluxes and distribution of water and sediment can have disproportionally large effects on the lateral channel mobility and thus lateral erosion rates (Bufe et al., 2016). Therefore, whereas no evidence for major changes in sediment and water fluxes or the flood frequency can be found, we hypothesize that small variations in these variables that are not coeval across the region drive large differences in the lateral erosion rates.

6.3.2. Planation in Different Catchments

Folds are beveled both by single large rivers, such as the Baishikeremuhe crossing the Kashi fold (Figures 3 and 7b), and by suites of braided streams migrating across the entire width of the fold, such as seen on the alluvial fans upstream of Atushi and Mutule (Figure 7). Notably, efficient beveling of these two folds has been accomplished by rivers with $>$40-fold differences in drainage areas ($<$100 km^2 to 4,000 km^2) even though bedrock strength, rock-uplift rates, and climatic conditions are fairly homogenous across the study area. Therefore, similarly wide areas can be eroded, despite expected 10- to 100-fold differences in water discharges: an unexpected result. The small catchments with short (~5–6 km long), steep (2.5–3.5°), alluvial fans upstream of Mutule (Figures 4 and 5m–5o) must have had lateral erosion rates similar to larger streams on the longer (9 to 12 km long), gentler (1–1.5°) alluvial fans upstream western central Atushi (Figures 5g and 5h) during times of planation. At the same time, some large catchments only bevel relatively small proportions of the structures they cross: for example, the Baishikeremuhe crossing the Kashi fold (Figures 3 and 6).

A possible explanation for the discrepancy between different catchments is the dependence of fold planation on the lateral channel mobility of the antecedent rivers (Bufe et al., 2016). Given the $>$60-fold difference in upstream catchment area, we hypothesize that the lower discharge, and thus, smaller flow depth (Parker, 1978; Parker et al., 2007) of the rivers draining across Mutule is compensated by a higher sediment-to-water ratio and corresponding higher channel mobility (Bufe et al., 2016; Constantine et al., 2014; Wickert et al., 2013). The approximately twofold steeper slope of the Mutule fans (2.5–3.5°) compared to the fans on Atushi (1–1.5°) (Figures 5g and 5h versus 5m–5o) is consistent with a higher sediment-to-water ratio in the Mutule rivers (Ashworth et al., 2004; Bryant et al., 1995; Cazanacli et al., 2002; Kim et al., 2010; Whipple et al., 1998). Moreover, differences in lateral erosion efficiency between neighboring catchments could be due to small, random (autogenic) differences in sediment and water fluxes, differences in the upstream confinement of the river (Bufe et al., 2016), or differences between the flood magnitudes and frequencies in small and large catchments.

The relatively small size of planation surfaces on Kashi could be attributed to a lower mobility of the river due to some upstream boundary condition confining the flow of the Baishikeremuhe as it is draining across the westernmost Atushi fold (Bufe et al., 2016). However, the estimated lateral erosion rates during beveling of the main T4 terrace are on the same order or even higher than those on Mutule and Atushi (Table 7). Another possible explanation for the lack of complete beveling is the faster uplift rate of the Kashi fold compared to the Atushi and Mutule folds. Finally, the relatively late capture of the Baishikeremuhe (Chen et al., 2007) or the perhaps quite sustained diversion of significant discharge around the nose of the eastern Kashi fold (Chen et al., 2007; Scharer et al., 2006) could inhibit a more complete beveling of the Kashi fold. Finally, if the topography of the Kashi fold had been high (>10–100 m) at the time of capture, the presence of high walls may have slowed lateral erosion (Malatesta et al., 2016). Similar topographic thresholds could inhibit renewed planation of eastern Atushi (Figure 7d).

7. Conclusion

Despite rapid rock-uplift rates of 1–3 mm/yr over the past 30–80 kyr, actively uplifting folds in the foreland of the Tian Shan have been efficiently and extensively beveled by antecedent rivers. In striking contrast, modern rivers incise narrow canyons into the uplifting structures. These observations imply temporal changes in the ratio of lateral to vertical erosion rates. In order to explain the beveled platforms merely with changes in incision rates, pauses of rock uplift and related incision of 30–140 kyr would be necessary. Such long pauses in uplift or similarly long phases of aggradation that outpace uplift rates seem impossible to reconcile with our observations. We, therefore, argue that changes in lateral erosion rates are necessary to explain the existence of the planation surfaces in the Tian Shan. In the likely case where average incision rates remain fairly steady when timescales of >2–6 kyr are considered, average lateral bedrock erosion rates have to be at least 200–600 mm/yr during episodes of active planation of the folds: rates that are 70 to 600 times higher than the average vertical incision rates. These estimates are minima, and planation rates could be as high as several meters per year. In contrast to these intervals of rapid lateral beveling, order-of-magnitude decreases in these rates seem to be required to explain the formation of the relatively narrow bedrock canyons that dominate today. A link of the intermittent episodes of planation and incision to climatic cycles is unclear. We hypothesize that small, local changes in water and sediment fluxes or the frequency of flooding events may have large effects on the lateral channel mobility of the streams and, therefore, on fold planation. We propose that changes in the average rates of lateral erosion by rivers are the primary control on the formation of fluvial planation surfaces in the foreland of the Tian Shan. Whereas lateral erosion rates probably partly covary with vertical incision rates, changes in the latter seem unimportant in controlling the size of the studied planation surfaces. In other tectonic settings with slower rock-uplift rates and/or harder bedrock lithologies, vertical erosion-rate changes are likely more important. However, we hypothesize that the variability of lateral erosion rates exerts a critical control on the size, rates, and timing of strath-terrace formation in other areas—especially those with readily eroded bedrock.

Notations

Parameters

- A plan view area created by lateral erosion (m^2).
- D depth of incised valley (m).
- E_h average horizontal (lateral) erosion rate (m yr^{-1}).
- E_v average vertical erosion (incision) rate (m yr^{-1}).
- G surface uplift rate due to sediment aggradation (m yr^{-1}).
- H maximum height difference across strath surface (m).
- L length of eroded surface in the average flow direction (m).
- P areal planation rate (m^2 yr^{-1}).
- U rock-uplift rate (m yr^{-1}).
- Δt duration of incision or beveling episode (year).

Subscripts

- b beveling episode.
- i incision episode.

Acknowledgments
This work was supported by National Science Foundation grant 1050070 to D. W. B. and B. B. and the LED2016A05, NSFC grant 41772221 to C. J., L. T., Q. J., Y. H., and L. L. Extensive and thoughtful reviews by Frank J. Pazzaglia, two anonymous reviewers, and Editors Noah Finnegan, Mikaël Attal, and John M. Buffington improved an earlier version of the manuscript. In addition, the work benefited from discussions with Thomas Dunne. Imbrication measurements, lithological clast counts, clast-size counts, structural data for the Mutule fold, and the raw data for OSL and CRN dating can be found in Tables S1–S8. Mapped terraces, beveled areas, and GPS surveys are included as shapefiles in the supporting information.

References

Abdrakhmatov, K. Y., Aldazhanov, S. A., Hager, B. H., Hamburger, M. W., Herring, T. A., Kalabaev, K. B., … Zubovich, A. V. (1996). Relatively recent construction of the Tien Shan inferred from GPS measurements of present-day crustal deformation rates. *Nature*, *384*(6608), 450–453. https://doi.org/10.1038/384450a0

Allen, G. H., Barnes, J. B., Pavelsky, T. M., & Kirby, E. (2013). Lithologic and tectonic controls on bedrock channel form at the northwest Himalayan front. *Journal of Geophysical Research: Earth Surface*, *118*, 1806–1825. https://doi.org/10.1002/jgrf.20113

Amos, C. B., Burbank, D. W., Nobes, D. C., & Read, S. A. L. (2007). Geomorphic constraints on listric thrust faulting: Implications for active deformation in the Mackenzie Basin, South Island, New Zealand. *Journal of Geophysical Research*, *112*, B03S11. https://doi.org/10.1029/2006JB004291

Anderson, R. S., Repka, J. L., & Dick, G. S. (1996). Explicit treatment of inheritance in dating depositional surfaces using in situ ^{10}Be and ^{26}Al. *Geology*, *24*(1), 47–51. https://doi.org/10.1130/0091-7613(1996)024%3C0047:etoiid%3E2.3.co;2

Anton, L., Mather, A. E., Stokes, M., Munoz-Martin, A., & De Vicente, G. (2015). Exceptional river gorge formation from unexceptional floods. *Nature Communications*, *6*, 7963. https://doi.org/10.1038/ncomms8963

Arnold, L. J., Bailey, R. M., & Tucker, G. E. (2007). Statistical treatment of fluvial dose distributions from southern Colorado arroyo deposits. *Quaternary Geochronology*, *2*(1-4), 162–167. https://doi.org/10.1016/j.quageo.2006.05.003

Ashworth, P. J., Best, J. L., & Jones, M. (2004). Relationship between sediment supply and avulsion frequency in braided rivers. *Geology*, *32*, 21–24. https://doi.org/10.1130/g19919.1

Bailey, R. M., & Arnold, L. J. (2006). Statistical modelling of single grain quartz De distributions and an assessment of procedures for estimating burial dose. *Quaternary Science Reviews*, *25*, 2475–2502. https://doi.org/10.1016/j.quascirev.2005.09.012

Balco, G., Stone, J. O., Lifton, N. A., & Dunai, T. J. (2008). A complete and easily accessible means of calculating surface exposure ages or erosion rates from 10Be and ^{26}Al measurements. *Quaternary Geochronology*, *3*, 174–195. https://doi.org/10.1016/j.quageo.2007.12.001

Bande, A., Sobel, E. R., Mikolaichuk, A., Schmidt, A., & Stockli, D. F. (2017). Exhumation history of the western Kyrgyz Tien Shan: Implications for intramontane basin formation. *Tectonics*, *36*(1), 163–180. https://doi.org/10.1002/2016TC004284

Bazhenov, M. L., Collins, A. Q., Degtyarev, K. E., Levashova, N. M., Mikolaichuk, A. V., Pavlov, V. E., & Van der Voo, R. (2003). Paleozoic northward drift of the North Tien Shan (central Asia) as revealed by Ordovician and Carboniferous paleomagnetism. *Tectonophysics*, *366*(1-2), 113–141. https://doi.org/10.1016/S0040-1951(03)00075-1

Beer, A. R., Turowski, J. M., & Kirchner, J. W. (2017). Spatial patterns of erosion in a bedrock gorge. *Journal of Geophysical Research: Earth Surface*, *122*, 191–214. https://doi.org/10.1002/2016JF003850

Bookhagen, B., Fleitmann, D., Nishiizumi, K., Strecker, M. R., & Thiede, R. C. (2006). Holocene monsoonal dynamics and fluvial terrace formation in the northwest Himalaya, India. *Geology*, *34*, 601–604. https://doi.org/10.1130/g22698.1

Bookhagen, B., & Strecker, M. R. (2012). Spatiotemporal trends in erosion rates across a pronounced rainfall gradient: Examples from the southern Central Andes. *Earth and Planetary Science Letters*, *327-328*, 97–110. https://doi.org/10.1016/j.epsl.2012.02.005

Borchers, B., Marrero, S., Balco, G., Caffee, M., Goehring, B., Lifton, N., … Stone, J. (2016). Geological calibration of spallation production rates in the CRONUS-Earth project. *Quaternary Geochronology*, *31*, 188–198. https://doi.org/10.1016/j.quageo.2015.01.009

Brocard, G. Y., & van der Beek, P. A. (2006). Influence of incision rate, rock strength, and bedload supply on bedrock river gradients and valley-flat widths: Field-based evidence and calibrations from western Alpine rivers (southeast France). In S. D. Willett, et al. (Eds.), *Tectonics, Climate, and Landscape Evolution*, *Geological Society of America Special Paper* (Vol. 398, pp. 101–126). Geological Society of America.

Bryant, M., Falk, P., & Paola, C. (1995). Experimental study of avulsion frequency and rate of deposition. *Geology*, *23*(4), 365–368. https://doi.org/10.1130/0091-7613(1995)023%3C0365:esoafa%3E2.3.co;2

Bufe, A., Bekaert, D. P. S., Hussain, E., Bookhagen, B., Burbank, D. W., Thompson Jobe, J. A., … Gan, W. (2017). Temporal changes in rock-uplift rates of folds in the foreland of the Tian Shan and the Pamir from geodetic and geologic data. *Geophysical Research Letters*, *44*. https://doi.org/10.1002/2017GL073627

Bufe, A., Paola, C., & Burbank, D. W. (2016). Fluvial bevelling of topography controlled by lateral channel mobility and uplift rate. *Nature Geoscience*, *9*(9), 706–710. https://doi.org/10.1038/ngeo2773

Bull, W. B. (1990). Stream-terrace genesis: Implications for soil development. *Geomorphology*, *3*(3-4), 351–367. https://doi.org/10.1016/0169-555X(90)90011-E

Burbank, D. W., Leland, J., Fielding, E., Anderson, R. S., Brozovic, N., Reid, M. R., & Duncan, C. (1996). Bedrock incision, rock uplift and threshold hillslopes in the northwestern Himalayas. *Nature*, *379*(6565), 505–510. https://doi.org/10.1038/379505a0

Calvet, M., Gunnell, Y., & Farines, B. (2015). Flat-topped mountain ranges: Their global distribution and value for understanding the evolution of mountain topography. *Geomorphology*, *241*, 255–291. https://doi.org/10.1016/j.geomorph.2015.04.015

Carroll, A. R., Graham, S. A., Hendrix, M. S., Ying, D., & Zhou, D. (1995). Late Paleozoic tectonic amalgamation of northwestern China: Sedimentary record of the northern Tarim, northwestern Turpan, and southern Junggar Basins. *Geological Society of America Bulletin*, *107*(5), 571–594. https://doi.org/10.1130/0016-7606(1995)107%3C0571:lptaon%3E2.3.co;2

Castillo, M., Bishop, P., & Jansen, J. D. (2013). Knickpoint retreat and transient bedrock channel morphology triggered by base-level fall in small bedrock river catchments: The case of the Isle of Jura, Scotland. *Geomorphology*, *180-181*, 1–9. https://doi.org/10.1016/j.geomorph.2012.08.023

Cazanacli, D., Paola, C., & Parker, G. (2002). Experimental steep, braided flow: Application to flooding risk on fans. *Journal of Hydrologic Engineering*, *128*(3), 322–330. https://doi.org/10.1061/(ASCE)0733-9429(2002)128:3(322)

Charreau, J., Gumiaux, C., Avouac, J.-P., Augier, R., Chen, Y., Barrier, L., … Wang, Q. (2009). The Neogene Xiyu Formation, a diachronous prograding gravel wedge at front of the Tianshan: Climatic and tectonic implications. *Earth and Planetary Science Letters*, *287*, 298–310. https://doi.org/10.1016/j.epsl.2009.07.035

Chen, J., Burbank, D. W., Scharer, K. M., Sobel, E., Yin, J., Rubin, C., & Zhao, R. (2002). Magnetochronology of the upper Cenozoic strata in the southwestern Chinese Tian Shan: Rates of Pleistocene folding and thrusting. *Earth and Planetary Science Letters*, *195*(1-2), 113–130. https://doi.org/10.1016/S0012-821X(01)00579-9

Chen, J., Heermance, R., Burbank, D. W., Scharer, K. M., Miao, J., & Wang, C. (2007). Quantification of growth and lateral propagation of the Kashi anticline, southwest Chinese Tian Shan. *Journal of Geophysical Research*, *112*, B03S16. https://doi.org/10.1029/2006JB004345

Chmeleff, J., von Blanckenburg, F., Kossert, K., & Jakob, D. (2010). Determination of the ^{10}Be half-life by multicollector ICP-MS and liquid scintillation counting. *Nuclear Instruments and Methods in Physics Research Section B: Beam Interactions with Materials and Atoms*, *268*, 192–199. https://doi.org/10.1016/j.nimb.2009.09.012

Collins, B. D., Montgomery, D. R., Schanz, S. A., & Larsen, I. J. (2016). Rates and mechanisms of bedrock incision and strath terrace formation in a forested catchment, Cascade Range, Washington. *Geological Society of America Bulletin*, *128*(5-6), 926–943. https://doi.org/10.1130/b31340.1

Constantine, J. A., Dunne, T., Ahmed, J., Legleiter, C., & Lazarus, E. D. (2014). Sediment supply as a driver of river meandering and floodplain evolution in the Amazon Basin. *Nature Geoscience*, *7*(12), 899–903. https://doi.org/10.1038/ngeo2282

Cook, K. L., Turowski, J. M., & Hovius, N. (2013). A demonstration of the importance of bedload transport for fluvial bedrock erosion and knickpoint propagation. *Earth Surface Processes and Landforms*, *38*(7), 683–695. https://doi.org/10.1002/esp.3313

Cook, K. L., Turowski, J. M., & Hovius, N. (2014). River gorge eradication by downstream sweep erosion. *Nature Geoscience*, *7*(9), 682–686. https://doi.org/10.1038/ngeo2224

Coutand, I., Strecker, M. R., Arrowsmith, J. R., Hilley, G., Thiede, R. C., Korjenkov, A., & Omuraliev, M. (2002). Late Cenozoic tectonic development of the intramontane Alai Valley, (Pamir-Tien Shan region, central Asia): An example of intracontinental deformation due to the indo-Eurasia collision. *Tectonics*, *21*(6), 1053. https://doi.org/10.1029/2002TC001358

Davis, M., Matmon, A., Rood, D. H., & Avnaim-Katav, S. (2012). Constant cosmogenic nuclide concentrations in sand supplied from the Nile River over the past 2.5 m.y. *Geology*, *40*, 359–362. https://doi.org/10.1130/g32574.1

Davis, W. M. (1902). Baselevel, grade and peneplain. *Journal of Geology*, *10*(1), 77–111. https://doi.org/10.2307/30055546

DeVecchio, D. E., Heermance, R. V., Fuchs, M., & Owen, L. A. (2012). Climate-controlled landscape evolution in the western Transverse Ranges, California: Insights from Quaternary geochronology of the Saugus Formation and strath terrace flights. *Lithosphere US*, *4*, 110–130. https://doi.org/10.1130/l176.1

Dey, S., Thiede, R. C., Schildgen, T. F., Wittmann, H., Bookhagen, B., Scherler, D., … Strecker, M. R. (2016). Climate-driven sediment aggradation and incision since the late Pleistocene in the NW Himalaya, India. *Earth and Planetary Science Letters*, *449*, 321–331. https://doi.org/10.1016/j.epsl.2016.05.050

DiBiase, R. A., & Whipple, K. X. (2011). The influence of erosion thresholds and runoff variability on the relationships among topography, climate, and erosion rate. *Journal of Geophysical Research*, *116*, F04036. https://doi.org/10.1029/2011JF002095

Dietrich, W. E., Bellugi, D. G., Sklar, L. S., Stock, J. D., Heimsath, A. M., & Roering, J. J. (2003). Geomorphic transport laws for predicting landscape form and dynamics. In *Prediction in Geomorphology* (pp. 103–132). Washington, DC: American Geophysical Union. https://doi.org/10.1029/135GM09

Dietrich, W. E., Kirchner, J. W., Ikeda, H., & Iseya, F. (1989). Sediment supply and the development of the coarse surface layer in gravel-bedded rivers. *Nature*, *340*(6230), 215–217. https://doi.org/10.1038/340215a0

Finnegan, N. J., & Balco, G. (2013). Sediment supply, base level, braiding, and bedrock river terrace formation: Arroyo Seco, California, USA. *Geological Society of America Bulletin*, *125*(7-8), 1114–1124. https://doi.org/10.1130/B30727.1

Finnegan, N. J., & Dietrich, W. E. (2011). Episodic bedrock strath terrace formation due to meander migration and cutoff. *Geology*, *39*(2), 143–146. https://doi.org/10.1130/G31716.1

Formento-Trigilio, M. L., Burbank, D. W., Nicol, A., Shulmeister, J., & Rieser, U. (2003). River response to an active fold-and-thrust belt in a convergent margin setting, North Island, New Zealand. *Geomorphology*, *49*(1-2), 125–152. https://doi.org/10.1016/S0169-555X(02)00167-8

Fuller, T. K., Gran, K. B., Sklar, L. S., & Paola, C. (2016). Lateral erosion in an experimental bedrock channel: The influence of bed roughness on erosion by bed-load impacts. *Journal of Geophysical Research: Earth Surface*, *121*, 1084–1105. https://doi.org/10.1002/2015JF003728

Fuller, T. K., Perg, L. A., Willenbring, J. K., & Lepper, K. (2009). Field evidence for climate-driven changes in sediment supply leading to strath terrace formation. *Geology*, *37*, 467–470. https://doi.org/10.1130/g25487a.1

Galbraith, R. F. (2005). *Statistics for fission track analysis*. Boca Raton, FL: Chapman and Hall/CRC.

Galbraith, R. F., & Roberts, R. G. (2012). Statistical aspects of equivalent dose and error calculation and display in OSL dating: An overview and some recommendations. *Quaternary Geochronology*, *11*, 1–27. https://doi.org/10.1016/j.quageo.2012.04.020

Galbraith, R. F., Roberts, R. G., Laslett, G. M., Yoshida, H., & Olley, J. M. (1999). Optical dating of single and multiple grains of quartz from Jinmium Rock Shelter, northern Australia: Part I. Experimental design and statistical models. *Archaeometry*, *41*(2), 339–364. https://doi.org/10.1111/j.1475-4754.1999.tb00987.x

Gao, R., Hou, H., Cai, X., Knapp, J. H., He, R., Liu, J., … Roecker, S. W. (2013). Fine crustal structure beneath the junction of the southwest Tian Shan and Tarim Basin, NW China. *Lithosphere US.*, *5*(4), 382–392. https://doi.org/10.1130/l248.1

Gilbert, G. K. (1877). *Report on the Geology of the Henry Mountains (Utah)*. Washington, DC: Government Printing Office.

Gorokhovich, Y., & Voustianiouk, A. (2006). Accuracy assessment of the processed SRTM-based elevation data by CGIAR using field data from USA and Thailand and its relation to the terrain characteristics. *Remote Sensing of Environment*, *104*(4), 409–415. https://doi.org/10.1016/j.rse.2006.05.012

Gosse, J. C., & Phillips, F. M. (2001). Terrestrial in situ cosmogenic nuclides: Theory and application. *Quaternary Science Reviews*, *20*(14), 1475–1560. https://doi.org/10.1016/S0277-3791(00)00171-2

Grimaud, J. L., Paola, C., & Voller, V. (2016). Experimental migration of knickpoints: Influence of style of base-level fall and bed lithology. *Earth Surface Dynamics*, *4*(1), 11–23. https://doi.org/10.5194/esurf-4-11-2016

Gunderson, K. L., Pazzaglia, F. J., Picotti, V., Anastasio, D. A., Kodama, K. P., Rittenour, T., … Sabbatini, A. (2014). Unraveling tectonic and climatic controls on synorogenic growth strata (northern Apennines, Italy). *Geological Society of America Bulletin*, *126*(3-4), 532–552. https://doi.org/10.1130/b30902.1

Hack, J. T. (1957). Studies of longitudinal stream profiles in Virginia and Maryland, Report Rep. 294B.

Hancock, G. S., & Anderson, R. S. (2002). Numerical modeling of fluvial strath-terrace formation in response to oscillating climate. *Geological Society of America Bulletin*, *114*(9), 1131–1142. https://doi.org/10.1130/0016-7606(2002)114%3C1131:nmofst%3E2.0.co;2

Hancock, G. S., Anderson, R. S., Chadwick, O. A., & Finkel, R. C. (1999). Dating fluvial terraces with ^{10}Be and ^{26}Al profiles: Application to the Wind River, Wyoming. *Geomorphology*, *27*(1-2), 41–60. https://doi.org/10.1016/S0169-555X(98)00089-0

Hanson, P. R., Mason, J. A., & Goble, R. J. (2006). Fluvial terrace formation along Wyoming's Laramie range as a response to increased late Pleistocene flood magnitudes. *Geomorphology*, *76*, 12–25. https://doi.org/10.1016/j.geomorph.2005.08.010

Hartshorn, K., Hovius, N., Dade, W. B., & Slingerland, R. L. (2002). Climate-driven bedrock incision in an active mountain belt. *Science*, *297*(5589), 2036–2038. https://doi.org/10.1126/science.1075078

Heermance, R. V., Chen, J., Burbank, D. W., & Miao, J. (2008). Temporal constraints and pulsed late Cenozoic deformation during the structural disruption of the active Kashi foreland, northwest China. *Tectonics*, *27*, TC6012. https://doi.org/10.1029/2007TC002226

Heermance, R. V., Chen, J., Burbank, D. W., & Wang, C. (2007). Chronology and tectonic controls of late Tertiary deposition in the southwestern Tian Shan foreland, NW China. *Basin Research*, *19*, 599–632. https://doi.org/10.1111/j.1365-2117.2007.00339.x

Hendrix, M. S., Graham, S. A., Carroll, A. R., Sobel, E. R., Mcknight, C. L., Schulein, B. J., & Wang, Z. X. (1992). Sedimentary record and climatic implications of recurrent deformation in the Tian-Shan—Evidence from Mesozoic strata of the North Tarim, South Junggar, and Turpan Basins, Northwest China. *Geological Society of America Bulletin*, *104*(1), 53–79. https://doi.org/10.1130/0016-7606(1992)104%3C0053:Sracio%3E2.3.Co;2

Hidy, A. J., Gosse, J. C., Blum, M. D., & Gibling, M. R. (2014). Glacial–interglacial variation in denudation rates from interior Texas, USA, established with cosmogenic nuclides. *Earth and Planetary Science Letters*, *390*, 209–221. https://doi.org/10.1016/j.epsl.2014.01.011

Hidy, A. J., Gosse, J. C., Pederson, J. L., Mattern, J. P., & Finkel, R. C. (2010). A geologically constrained Monte Carlo approach to modeling exposure ages from profiles of cosmogenic nuclides: An example from Lees Ferry, Arizona. *Geochemistry, Geophysics, Geosystems*, *11*, Q0AA10. https://doi.org/10.1029/2010GC003084

Jansen, J. D., Fabel, D., Bishop, P., Xu, S., Schnabel, C., & Codilean, A. T. (2011). Does decreasing paraglacial sediment supply slow knickpoint retreat? *Geology*, *39*(6), 543–546. https://doi.org/10.1130/g32018.1

Jarvis, A., Reuter, H. I., Nelson, A., & Guevara, E. (2008). Hole-filled SRTM for the globe version 4, available from the CGIAR-CSI SRTM 90m Database (http://srtm.csi.cgiar.org)

Jerolmack, D. J., & Mohrig, D. (2007). Conditions for branching in depositional rivers. *Geology*, *35*(5), 463–466. https://doi.org/10.1130/g23308a.1

Jia, Y., Fu, B., Jolivet, M., & Zheng, S. (2015). Cenozoic tectono-geomorphological growth of the SW Chinese Tian Shan: Insight from AFT and detrital zircon U–Pb data. *Journal of Asian Earth Sciences*, *111*, 395–413. https://doi.org/10.1016/j.jseaes.2015.06.023

Johnson, J. P., & Whipple, K. X. (2007). Feedbacks between erosion and sediment transport in experimental bedrock channels. *Earth Surface Processes and Landforms*, *32*(7), 1048–1062. https://doi.org/10.1002/esp.1471

Johnson, J. P. L., & Whipple, K. X. (2010). Evaluating the controls of shear stress, sediment supply, alluvial cover, and channel morphology on experimental bedrock incision rate. *Journal of Geophysical Research*, *115*, F02018. https://doi.org/10.1029/2009JF001335

Kenworthy, M. K., Rittenour, T. M., Pierce, J. L., Sutfin, N. A., & Sharp, W. D. (2014). Luminescence dating without sand lenses: An application of OSL to coarse-grained alluvial fan deposits of the Lost River Range, Idaho, USA. *Quaternary Geochronology*, *23*, 9–25. https://doi.org/10.1016/j.quageo.2014.03.004

Kim, W., Sheets, B. A., & Paola, C. (2010). Steering of experimental channels by lateral basin tilting. *Basin Research*, *22*(3), 286–301. https://doi.org/10.1111/j.1365-2117.2009.00419.x

Kirby, E., & Whipple, K. X. (2012). Expression of active tectonics in erosional landscapes. *Journal of Structural Geology*, *44*, 54–75. https://doi.org/10.1016/j.jsg.2012.07.009

Korschinek, G., Bergmaier, A., Faestermann, T., Gerstmann, U. C., Knie, K., Rugel, G., … Remmert, A. (2010). A new value for the half-life of ^{10}Be by heavy-ion elastic recoil detection and liquid scintillation counting. *Nuclear Instruments and Methods in Physics Research Section B: Beam Interactions with Materials and Atoms*, *268*(2), 187–191. https://doi.org/10.1016/j.nimb.2009.09.020

Kurth, G., Phillips, F. M., Reheis, M. C., Redwine, J. L., & Paces, J. B. (2011). Cosmogenic nuclide and uranium-series dating of old, high shorelines in the western Great Basin, USA. *Geological Society of America Bulletin*, *123*(3-4), 744–768. https://doi.org/10.1130/b30010.1

Labourdette, R., & Jones, R. R. (2007). Characterization of fluvial architectural elements using a three-dimensional outcrop data set: Escanilla braided system, south-central Pyrenees, Spain. *Geosphere*, *3*(6), 422–434. https://doi.org/10.1130/ges00087.1

Lague, D. (2014). The stream power river incision model: Evidence, theory and beyond. *Earth Surface Processes and Landforms*, *39*(1), 38–61. https://doi.org/10.1002/esp.3462

Lague, D., Crave, A., & Davy, P. (2003). Laboratory experiments simulating the geomorphic response to tectonic uplift. *Journal of Geophysical Research*, *108*(B1), 2008. https://doi.org/10.1029/2002JB001785

Lal, D. (1991). Cosmic ray labeling of erosion surfaces: In situ nuclide production rates and erosion models. *Earth and Planetary Science Letters*, *104*(2-4), 424–439. https://doi.org/10.1016/0012-821X(91)90220-C

Langston, A. L., Tucker, G. E., & Anderson, R. S. (2015). Interpreting climate-modulated processes of terrace development along the Colorado Front Range using a landscape evolution model. *Journal of Geophysical Research: Earth Surface*, *120*, 2121–2138. https://doi.org/10.1002/2014JF003403

Lavé, J., & Avouac, J. P. (2001). Fluvial incision and tectonic uplift across the Himalayas of central Nepal. *Journal of Geophysical Research*, *106*(B11), 26,561–26,591. https://doi.org/10.1029/2001JB000359

Li, T., Chen, J., Thompson, J. A., Burbank, D. W., & Xiao, W. (2012). Equivalency of geologic and geodetic rates in contractional orogens: New insights from the Pamir Frontal Thrust. *Geophysical Research Letters*, *39*, L15305. https://doi.org/10.1029/2012GL051782

Li, T., Chen, J., Thompson, J. A., Burbank, D. W., & Yang, X. (2013). Quantification of three-dimensional folding using fluvial terraces: A case study from the Mushi anticline, northern margin of the Chinese Pamir. *Journal of Geophysical Research: Earth Surface*, *118*, 4628–4647. https://doi.org/10.1002/jgrb.50316

Li, T., Chen, J., Thompson, J. A., Burbank, D. W., & Yang, H. (2015a). Hinge-migrated fold-scarp model based on an analysis of bed geometry: A study from the Mingyaole anticline, southern foreland of Chinese Tian Shan. *Journal of Geophysical Research: Earth Surface*, *120*, 6592–6613. https://doi.org/10.1002/2015JB012102

Li, T., Chen, J., Thompson, J. A., Burbank, D. W., & Yang, X. (2015b). Active flexural-slip faulting: A study from the Pamir-Tian Shan convergent zone, NW China. *Journal of Geophysical Research: Earth Surface*, *120*, 4359–4378. https://doi.org/10.1002/2014JB011632

Lifton, N., Sato, T., & Dunai, T. J. (2014). Scaling in situ cosmogenic nuclide production rates using analytical approximations to atmospheric cosmic-ray fluxes. *Earth and Planetary Science Letters*, *386*, 149–160. https://doi.org/10.1016/j.epsl.2013.10.052

Limaye, A. B. S., & Lamb, M. P. (2014). Numerical simulations of bedrock valley evolution by meandering rivers with variable bank material. *Journal of Geophysical Research: Earth Surface*, *119*, 927–950. https://doi.org/10.1002/2013JF002997

Limaye, A. B. S., & Lamb, M. P. (2016). Numerical model predictions of autogenic fluvial terraces and comparison to climate change expectations. *Journal of Geophysical Research: Earth Surface*, *121*, 512–544. https://doi.org/10.1002/2014JF003392

Lisiecki, L. E., & Raymo, M. E. (2005). A Pliocene-Pleistocene stack of 57 globally distributed benthic δ^{18}O records. *Paleoceanography*, *20*, PA1003. https://doi.org/10.1029/2004PA001071

Mackin, H. J. (1948). Concept of the graded river. *Geological Society of America Bulletin*, *59*(5), 463–512. https://doi.org/10.1130/0016-7606(1948)59%5B463:cotgr%5D2.0.co;2

Malatesta, L. C., Prancevic, J. P., & Avouac, J.-P. (2016). Autogenic entrenchment patterns and terraces due to coupling with lateral erosion in incising alluvial channels. *Journal of Geophysical Research: Earth Surface*, *122*, 335–355. https://doi.org/10.1002/2015JF003797

McPhillips, D., Bierman, P. R., Crocker, T., & Rood, D. H. (2013). Landscape response to Pleistocene-Holocene precipitation change in the Western Cordillera, Peru: ^{10}Be concentrations in modern sediments and terrace fills. *Journal of Geophysical Research: Earth Surface*, *118*, 2488–2499. https://doi.org/10.1002/2013JF002837

Merritts, D. J., Vincent, K. R., & Wohl, E. E. (1994). Long river profiles, tectonism, and eustasy: A guide to interpreting fluvial terraces. *Journal of Geophysical Research*, *99*(B7), 14,031–14,050. https://doi.org/10.1029/94JB00857

Miall, A. D. (1977). A review of the braided-river depositional environment. *Earth-Science Reviews*, *13*(1), 1–62. https://doi.org/10.1016/0012-8252(77)90055-1

Molnar, P., Brown, E. T., Clark Burchfiel, B., Deng, Q., Feng, X., Li, J., … You, H. (1994). Quaternary climate change and the formation of river terraces across growing anticlines on the north flank of the Tien Shan, China. *Journal of Geology*, *102*(5), 583–602. https://doi.org/10.2307/30068558

Molnar, P., & Tapponnier, P. (1975). Cenozoic tectonics of Asia: Effects of a continental collision. *Science*, *189*(4201), 419–426. https://doi.org/10.1126/science.189.4201.419

Montgomery, D. R. (2004). Observations on the role of lithology in strath terrace formation and bedrock channel width. *American Journal of Science*, *304*(5), 454–476. https://doi.org/10.2475/ajs.304.5.454

Montgomery, D. R., Panfil, M. S., & Hayes, S. K. (1999). Channel-bed mobility response to extreme sediment loading at Mount Pinatubo. *Geology*, *27*(3), 271–274. https://doi.org/10.1130/0091-7613(1999)027%3C0271:cbmrte%3E2.3.co;2

Murray, A. S., & Wintle, A. G. (2000). Luminescence dating of quartz using an improved single-aliquot regenerative-dose protocol. *Radiation Measurements*, *32*(1), 57–73. https://doi.org/10.1016/S1350-4487(99)00253-X

Nathan, R. P. (2010). *Numerical modelling of environmental dose rate and its application to trapped-charge dating*. Oxford, UK: University of Oxford.

Nelson, M. S., Gray, H. J., Johnson, J. A., Rittenour, T. M., Feathers, J. K., & Mahan, S. A. (2015). User guide for luminescence sampling in archaeological and geological contexts. *Advances in Archaeological Practice*, *3*(02), 166–177. https://doi.org/10.7183/2326-3768.3.2.166

Nishiizumi, K., Imamura, M., Caffee, M. W., Southon, J. R., Finkel, R. C., & McAninch, J. (2007). Absolute calibration of ^{10}Be AMS standards. *Nuclear Instruments and Methods in Physics Research Section B: Beam Interactions with Materials and Atoms*, *258*, 403–413. https://doi.org/10.1016/j.nimb.2007.01.297

Olley, J., Caitcheon, G., & Murray, A. (1998). The distribution of apparent dose as determined by optically stimulated luminescence in small aliquots of fluvial quartz: Implications for dating young sediments. *Quaternary Science Reviews*, *17*(11), 1033–1040. https://doi.org/10.1016/S0277-3791(97)00090-5

Olley, J. M., Caitcheon, G. G., & Roberts, R. G. (1999). The origin of dose distributions in fluvial sediments, and the prospect of dating single grains from fluvial deposits using optically stimulated luminescence. *Radiation Measurements*, *30*(2), 207–217. https://doi.org/10.1016/S1350-4487(99)00040-2

Olley, J. M., Murray, A., & Roberts, R. G. (1996). The effects of disequilibria in the uranium and thorium decay chains on burial dose rates in fluvial sediments. *Quaternary Science Reviews*, *15*(7), 751–760. https://doi.org/10.1016/0277-3791(96)00026-1

Olley, J. M., Pietsch, T., & Roberts, R. G. (2004). Optical dating of Holocene sediments from a variety of geomorphic settings using single grains of quartz. *Geomorphology*, *60*(3-4), 337–358. https://doi.org/10.1016/j.geomorph.2003.09.020

Olley, J. M., Roberts, R. G., & Murray, A. S. (1997). Disequilibria in the uranium decay series in sedimentary deposits at Allen's cave, nullarbor plain, Australia: Implications for dose rate determinations. *Radiation Measurements*, *27*(2), 433–443. https://doi.org/10.1016/S1350-4487(96)00114-X

Pan, B., Burbank, D., Wang, Y., Wu, G., Li, J., & Guan, Q. (2003). A 900 k.y. record of strath terrace formation during glacial-interglacial transitions in northwest China. *Geology*, *31*(11), 957–960. https://doi.org/10.1130/g19685.1

Parker, G. (1978). Self-formed straight rivers with equilibrium banks and mobile bed. Part 2. The gravel river. *Journal of Fluid Mechanics*, *89*(01), 127–146. https://doi.org/10.1017/S0022112078002505

Parker, G., Wilcock, P. R., Paola, C., Dietrich, W. E., & Pitlick, J. (2007). Physical basis for quasi-universal relations describing bankfull hydraulic geometry of single-thread gravel bed rivers. *Journal of Geophysical Research*, *112*, F04005. https://doi.org/10.1029/2006JF000549

Pazzaglia, F. J. (2013). 9.22 fluvial terraces A2 - Shroder. In J. F. Shroder (Ed.), *Treatise on Geomorphology* (pp. 379–412). San Diego, CA: Academic Press. https://doi.org/10.1016/B978-0-12-374739-6.00248-7

Pazzaglia, F. J., & Brandon, M. T. (2001). A fluvial record of long-term steady-state uplift and erosion across the Cascadia Forearc High, western Washington State. *American Journal of Science*, *301*(4-5), 385–431. https://doi.org/10.2475/ajs.301.4-5.385

Pazzaglia, F. J., & Gardner, T. W. (1993). Fluvial terraces of the lower Susquehanna River. *Geomorphology*, *8*(2-3), 83–113. https://doi.org/10.1016/0169-555X(93)90031-V

Pazzaglia, F. J., Gardner, T. W., & Merritts, D. J. (1998). Bedrock fluvial incision and longitudinal profile development over geologic time scales determined by fluvial terraces. In K. J. Tinkler & E. E. Wohl (Eds.), *Rivers over rock: Fluvial processes in bedrock channels* (pp. 207–235). Washington, DC: American Geophysical Union. https://doi.org/10.1029/GM107p0207

Petit, J. R., Jouzel, J., Raynaud, D., Barkov, N. I., Barnola, J.-M., Basile, I., … Stievenard, M. (1999). Climate and atmospheric history of the past 420,000 years from the Vostok ice core, Antarctica. *Nature*, *399*(6735), 429–436. http://www.nature.com/nature/journal/v399/n6735/suppinfo/399429a0_S1.html, https://doi.org/10.1038/20859

Pratt-Sitaula, B., Burbank, D. W., Heimsath, A., & Ojha, T. (2004). Landscape disequilibrium on 1000–10,000 year scales Marsyandi River, Nepal, central Himalaya. *Geomorphology*, *58*(1-4), 223–241. https://doi.org/10.1016/j.geomorph.2003.07.002

Prescott, J., & Hutton, J. (1988). Cosmic ray and gamma ray dosimetry for TL and ESR. *International Journal of Radiation Applications and Instrumentation. Part D. Nuclear Tracks and Radiation Measurements*, *14*(1-2), 223–227. https://doi.org/10.1016/1359-0189(88)90069-6

Prescott, J. R., & Hutton, J. T. (1994). Cosmic ray contributions to dose rates for luminescence and ESR dating: Large depths and long-term time variations. *Radiation Measurements*, *23*(2-3), 497–500. https://doi.org/10.1016/1350-4487(94)90086-8

Repka, J. L., Anderson, R. S., & Finkel, R. C. (1997). Cosmogenic dating of fluvial terraces, Fremont River, Utah. *Earth and Planetary Science Letters*, *152*, 59–73. https://doi.org/10.1016/S0012-821X(97)00149-0

Rhodes, E. J. (2011). Optically stimulated luminescence dating of sediments over the past 200,000 years. *Annual Review of Earth and Planetary Sciences*, *39*(1), 461–488. https://doi.org/10.1146/annurev-earth-040610-133425

Rittenour, T. M. (2008). Luminescence dating of fluvial deposits: Applications to geomorphic, palaeoseismic and archaeological research. *Boreas*, *37*(4), 613–635. https://doi.org/10.1111/j.1502-3885.2008.00056.x

Rodríguez, E., Morris, C. S., & Belz, J. E. (2006). A global assessment of the SRTM performance. *Photogrammetric Engineering & Remote Sensing*, *72*, 249–260. https://doi.org/10.14358/PERS.72.3.249

Rohrmann, A., Heermance, R., Kapp, P., & Cai, F. (2013). Wind as the primary driver of erosion in the Qaidam Basin, China. *Earth and Planetary Science Letters*, *374*, 1–10. https://doi.org/10.1016/j.epsl.2013.03.011

Römer, W. (2010). Multiple planation surfaces in basement regions: Implications for the reconstruction of periods of denudation and uplift in southern Zimbabwe. *Geomorphology*, *114*, 199–212. https://doi.org/10.1016/j.geomorph.2009.07.001

Schaller, M., Blanckenburg, F. V., Hovius, N., Veldkamp, A., van den Berg, M. W., & Kubik, P. W. (2004). Paleoerosion rates from cosmogenic ^{10}Be in a 1.3 Ma terrace sequence: Response of the river Meuse to changes in climate and rock uplift. *Journal of Geology*, *112*, 127–144. https://doi.org/10.1086/381654

Schaller, M., & Ehlers, T. A. (2006). Limits to quantifying climate driven changes in denudation rates with cosmogenic radionuclides. *Earth and Planetary Science Letters*, *248*, 153–167. https://doi.org/10.1016/j.epsl.2006.05.027

Schaller, M., von Blanckenburg, F., Veldkamp, A., Tebbens, L. A., Hovius, N., & Kubik, P. W. (2002). A 30 000 yr record of erosion rates from cosmogenic ^{10}Be in Middle European river terraces. *Earth and Planetary Science Letters*, *204*(1-2), 307–320. https://doi.org/10.1016/S0012-821X(02)00951-2

Schanz, S. A., & Montgomery, D. R. (2016). Lithologic controls on valley width and strath terrace formation. *Geomorphology*, *258*, 58–68. https://doi.org/10.1016/j.geomorph.2016.01.015

Scharer, K. M., Burbank, D. W., Chen, J., & Weldon, R. J. (2006). Kinematic models of fluvial terraces over active detachment folds: Constraints on the growth mechanism of the Kashi-Atushi fold system, Chinese Tian Shan. *Geological Society of America Bulletin*, *118*, 1006–1021. https://doi.org/10.1130/b25835.1

Scharer, K. M., Burbank, D. W., Chen, J., Weldon, R. J., Rubin, C., Zhao, R., & Shen, J. (2004). Detachment folding in the southwestern Tian Shan–Tarim foreland, China: Shortening estimates and rates. *Journal of Structural Geology*, *26*, 2119–2137. https://doi.org/10.1016/j.jsg.2004.02.016

Schildgen, T. F., Robinson, R. A. J., Savi, S., Phillips, W. M., Spencer, J. Q. G., Bookhagen, B., … Strecker, M. R. (2016). Landscape response to late Pleistocene climate change in NW Argentina: Sediment flux modulated by basin geometry and connectivity. *Journal of Geophysical Research: Earth Surface*, *121*, 392–414. https://doi.org/10.1002/2015JF003607

Schumm, S. A. (1969). River metamorphosis. *Journal of the Hydraulics Division*, *95*(1), 255–274.

Shepherd, R. G. (1972). Incised river meanders: Evolution in simulated bedrock. *Science*, *178*(4059), 409–411. https://doi.org/10.1126/science.178.4059.409

Sklar, L. S., & Dietrich, W. E. (2001). Sediment and rock strength controls on river incision into bedrock. *Geology*, *29*(12), 1087–1090. https://doi.org/10.1130/0091-7613(2001)029%3C1087:sarsco%3E2.0.co;2

Sklar, L. S., & Dietrich, W. E. (2004). A mechanistic model for river incision into bedrock by saltating bed load. *Water Resources Research*, *40*, W06301. https://doi.org/10.1029/2003WR002496

Sklar, L. S., & Dietrich, W. E. (2006). The role of sediment in controlling steady-state bedrock channel slope: Implications of the saltation–abrasion incision model. *Geomorphology*, *82*, 58–83. https://doi.org/10.1016/j.geomorph.2005.08.019

Sobel, E. R., & Dumitru, T. A. (1997). Thrusting and exhumation around the margins of the western Tarim basin during the India-Asia collision. *Journal of Geophysical Research*, *102*(B3), 5043–5063. https://doi.org/10.1029/96JB03267

Stark, C. P. (2006). A self-regulating model of bedrock river channel geometry. *Geophysical Research Letters*, *33*, L04402. https://doi.org/10.1029/2005GL023193

Stone, J. O. (2000). Air pressure and cosmogenic isotope production. *Journal of Geophysical Research*, *105*(B10), 23,753–23,759. https://doi.org/10.1029/2000JB900181

Stroeven, A. P., Hättestrand, C., Heyman, J., Kleman, J., & Morén, B. M. (2013). Glacial geomorphology of the Tian Shan. *Journal of Maps*, *9*(4), 505–512. https://doi.org/10.1080/17445647.2013.820879

Thompson Jobe, J. A., Tao, L., Chen, J., Burbank, D. W., & Bufe, A. (2017). Quaternary tectonic evolution of the Pamir-Tian Shan convergence zone, Northwest China. *Tectonics*, *36*. https://doi.org/10.1002/2017TC004541

Turowski, J. M., Hovius, N., Meng-Long, H., Lague, D., & Men-Chiang, C. (2008). Distribution of erosion across bedrock channels. *Earth Surface Processes and Landforms*, *33*, 353–363. https://doi.org/10.1002/esp.1559

Turowski, J. M., Lague, D., Crave, A., & Hovius, N. (2006). Experimental channel response to tectonic uplift. *Journal of Geophysical Research*, *111*, F03008. https://doi.org/10.1029/2005JF000306

Turowski, J. M., Lague, D., & Hovius, N. (2007). Cover effect in bedrock abrasion: A new derivation and its implications for the modeling of bedrock channel morphology. *Journal of Geophysical Research*, *112*, F04006. https://doi.org/10.1029/2006JF000697

Turowski, J. M., Lague, D., & Hovius, N. (2009). Response of bedrock channel width to tectonic forcing: Insights from a numerical model, theoretical considerations, and comparison with field data. *Journal of Geophysical Research*, *114*, F03016. https://doi.org/10.1029/2008JF001133

Wegmann, K. W., & Pazzaglia, F. J. (2002). Holocene strath terraces, climate change, and active tectonics: The Clearwater River basin, Olympic Peninsula, Washington State. *Geological Society of America Bulletin*, *114*(6), 731–744. https://doi.org/10.1130/0016-7606(2002)114%3C0731:hstcca%3E2.0.co;2

Wegmann, K. W., & Pazzaglia, F. J. (2009). Late Quaternary fluvial terraces of the Romagna and Marche Apennines, Italy: Climatic, lithologic, and tectonic controls on terrace genesis in an active orogen. *Quaternary Science Reviews*, *28*, 137–165. https://doi.org/10.1016/j.quascirev.2008.10.006

Wells, S. G., McFadden, L. D., Poths, J., & Olinger, C. T. (1995). Cosmogenic ^{3}He surface-exposure dating of stone pavements: Implications for landscape evolution in deserts. *Geology*, *23*(7), 613–616. https://doi.org/10.1130/0091-7613(1995)023%3C0613:chsedo%3E2.3.co;2

Whipple, K., Parker, G., Paola, C., & Mohrig, D. (1998). Channel dynamics, sediment transport, and the slope of alluvial fans: Experimental study. *Journal of Geology*, *106*(6), 677–694. https://doi.org/10.1086/516053

Whipple, K. X., & Tucker, G. E. (2002). Implications of sediment-flux-dependent river incision models for landscape evolution, *Journal of Geophysical Research*, *107*(B2), 2039. https://doi.org/10.1029/2000JB000044

Whittaker, A. C., Attal, M., & Allen, P. A. (2010). Characterising the origin, nature and fate of sediment exported from catchments perturbed by active tectonics. *Basin Research*, *22*, 809–828. https://doi.org/10.1111/j.1365-2117.2009.00447.x

Whittaker, A. C., Duller, R. A., Springett, J., Smithells, R. A., Whitchurch, A. L., & Allen, P. A. (2011). Decoding downstream trends in stratigraphic grain size as a function of tectonic subsidence and sediment supply. *Geological Society of America Bulletin*, *123*, 1363–1382. https://doi.org/10.1130/b30351.1

Wickert, A. D., Martin, J. M., Tal, M., Kim, W., Sheets, B., & Paola, C. (2013). River channel lateral mobility: Metrics, time scales, and controls. *Journal of Geophysical Research: Earth Surface*, *118*, 396–412. https://doi.org/10.1029/2012JF002386

Wintle, A. G., & Murray, A. S. (2006). A review of quartz optically stimulated luminescence characteristics and their relevance in single-aliquot regeneration dating protocols. *Radiation Measurements*, *41*, 369–391. https://doi.org/10.1016/j.radmeas.2005.11.001

Wittmann, H., von Blanckenburg, F., Maurice, L., Guyot, J.-L., Filizola, N., & Kubik, P. W. (2010). Sediment production and delivery in the Amazon River basin quantified by in situ—Produced cosmogenic nuclides and recent river loads. *Geological Society of America Bulletin*, *123*, 934–950. https://doi.org/10.1130/b30317.1

Wobus, C. W., Tucker, G. E., & Anderson, R. S. (2006). Self-formed bedrock channels. *Geophysical Research Letters*, *33*, L18408. https://doi.org/10.1029/2006GL027182

Wolman, M. G. (1954). A method of sampling coarse river-bed material. *Eos, Transactions of the American Geophysical Union*, *35*(6), 951–956. https://doi.org/10.1029/TR035i006p00951

Yang, Q., Wei, W., & Li, J. (2008). Temporal and spatial variation of atmospheric water vapor in the Taklimakan desert and its surrounding areas. *Chinese Science Bulletin*, *53*, 71–78. https://doi.org/10.1007/s11434-008-6007-2

Yang, X., & Scuderi, L. A. (2010). Hydrological and climatic changes in deserts of China since the late Pleistocene. *Quaternary Research*, *73*, 1–9. https://doi.org/10.1016/j.yqres.2009.10.011

Yanites, B. J., & Tucker, G. E. (2010). Controls and limits on bedrock channel geometry. *Journal of Geophysical Research*, *115*, F04019. https://doi.org/10.1029/2009JF001601

Yanites, B. J., Tucker, G. E., Mueller, K. J., & Chen, Y.-G. (2010). How rivers react to large earthquakes: Evidence from central Taiwan. *Geology*, *38*, 639–642. https://doi.org/10.1130/g30883.1

Yin, A., Nie, S., Craig, P., Harrison, T. M., Ryerson, F. J., Xianglin, Q., & Geng, Y. (1998). Late Cenozoic tectonic evolution of the southern Chinese Tian Shan. *Tectonics*, *17*(1), 1–27. https://doi.org/10.1029/97TC03140

Zander, A., Degering, D., Preusser, F., Kasper, H. U., & Brückner, H. (2007). Optically stimulated luminescence dating of sublittoral and intertidal sediments from Dubai, UAE: Radioactive disequilibria in the uranium decay series. *Quaternary Geochronology*, *2*, 123–128. https://doi.org/10.1016/j.quageo.2006.04.003

Zaprowski, B. J., Evenson, E. B., Pazzaglia, F. J., & Epstein, J. B. (2001). Knickzone propagation in the Black Hills and northern High Plains: A different perspective on the late Cenozoic exhumation of the Laramide Rocky Mountains. *Geology*, *29*(6), 547–550. https://doi.org/10.1130/0091-7613(2001)029%3C0547:kpitbh%3E2.0.co;2

Zhang, P.-Z., Shen, Z., Wang, M., Gan, W., Bürgmann, R., Molnar, P., … Xinzhao, Y. (2004). Continuous deformation of the Tibetan Plateau from global positioning system data. *Geology*, *32*, 809–812. https://doi.org/10.1130/g20554.1

Zubovich, A. V., Schöne, T., Metzger, S., Mosienko, O., Mukhamediev, S., Sharshebaev, A., & Zech, C. (2016). Tectonic interaction between the Pamir and Tien Shan observed by GPS. *Tectonics*, *35*(2), 283–292. https://doi.org/10.1002/2015TC004055

Zubovich, A. V., Wang, X.-q., Scherba, Y. G., Schelochkov, G. G., Reilinger, R., Reigber, C., … Beisenbaev, R. T. (2010). GPS velocity field for the Tien Shan and surrounding regions. *Tectonics*, *29*, TC6014. https://doi.org/10.1029/2010TC002772